

RED-PSM: Regularization by Denoising of Partially Separable Models for Dynamic Imaging

Berk Iskender¹ Marc L. Klasky² Yoram Bresler¹

¹University of Illinois at Urbana-Champaign, IL, USA ²Los Alamos National Laboratory, NM, USA

Abstract—Dynamic imaging addresses the recovery of a time-varying 2D or 3D object at each time instant using its under-sampled measurements. In particular, in the case of dynamic tomography, only a single projection at a single view angle may be available at a time, making the problem severely ill-posed. In this work, we propose an approach, RED-PSM, which combines for the first time two powerful techniques to address this challenging imaging problem. The first, are partially separable models, which have been used to efficiently introduce a low-rank prior for the spatio-temporal object. The second is the recent *Regularization by Denoising (RED)*, which provides a flexible framework to exploit the impressive performance of state-of-the-art image denoising algorithms, for various inverse problems. We propose a partially separable objective with RED and a computationally efficient and scalable optimization scheme with variable splitting and ADMM. Theoretical analysis proves the convergence of our objective to a value corresponding to a stationary point satisfying the first-order optimality conditions. Convergence is accelerated by a particular projection-domain-based initialization. We demonstrate the performance and computational improvements of our proposed RED-PSM with a learned image denoiser by comparing it to a recent deep-prior-based method known as TD-DIP. Although the main focus is on dynamic tomography, we also show performance advantages of RED-PSM in a cardiac dynamic MRI setting.

I. INTRODUCTION

TIME-VARYING or dynamic tomography involves the reconstruction of a dynamic object using its projections acquired sequentially in time. The problem arises in micro tomography [1], myocardial perfusion imaging [2], thoracic CT [3], imaging of fluid flow processes [4], [5] and dynamic imaging of material samples undergoing compression [6], [7]. Also, it is closely related to the dynamic MRI (dMRI) problem, which typically arises in cardiac imaging [8].

Dynamic tomography is a challenging ill-posed inverse problem: since the measurements are inconsistent due to the evolving object, traditional reconstruction algorithms lead to significant artifacts. As discussed further below, although numerous methods have been proposed to address this problem, they suffer from various limitations, or provide less than satisfactory reconstruction quality, especially in the scenario of main interest in this paper, when at each time instant only one projection is available.

A. Proposed Approach

We propose an approach, RED-PSM, which combines for the first time two powerful techniques to address this chal-

lenging imaging problem. The first, are partially separable models [9]–[16], which have been used before to efficiently introduce a low-rank prior for the spatio-temporal object. The second is the recent *Regularization by Denoising (RED)* [17], which provides a flexible framework to exploit the impressive performance of state-of-the-art image denoising algorithms, for various inverse problems.

We propose a partially separable objective with RED and a computationally efficient and scalable optimization scheme with variable splitting and ADMM.

Theoretical analysis proves the convergence of our objective to a value corresponding to a stationary point satisfying the first-order optimality conditions. Convergence is accelerated by a particular projection-domain-based initialization.

We demonstrate the performance and computational improvements of our proposed RED-PSM with a learned image denoiser by comparing it to a recent deep-prior-based method known as TD-DIP [18], and to spatial and spatiotemporal total variation (TV) regularized versions of PSM.

Although the main focus is on dynamic tomography, we also show performance advantages of RED-PSM in a cardiac dynamic MRI setting.

RED was originally inspired by the Plug-and-Play (PnP) approach [19], which was the first to exploit powerful denoisers to represent the prior on the object in inverse problems but without explicitly defining the regularizer. Instead, in PnP the denoiser is incorporated by replacing a proximal mapping. Both PnP and RED have shown strong empirical performance in various applications. A recent survey [20] provides a detailed discussion of the main results and different applications of PnP and the relation to RED. For the algorithmic variations PnP-ADMM and PnP-ISTA there are convergence results to unique fixed points. Moreover, for PnP-ISTA, similar to our result, convergence is shown to a stationary point of a possibly non-convex objective when the denoiser is an MMSE estimator [21]. This result requires the prior to be non-degenerate, i.e., not lie on a lower dimensional manifold, which, unfortunately, would be violated by the low-rank bilinear representation in our PSM. We believe that a PnP-based method similar to RED-PSM can be formulated for our problem, but a proof of convergence to a stationary point may not directly follow, and a different approach and analysis may be needed.

Our motivation for using the original RED formulation in RED-PSM rather than more recent formulations and analyses (e.g., as in [22] and the references therein) is based on its simple gradient expression, and explicit regularizer expression facilitating implementation and theoretical analysis.

*Corresponding email: berki2@illinois.edu

This research was supported in part by Los Alamos National Labs under Subcontract No. 599416/CW13995.

The objective is to demonstrate the large improvement in performance that this simple learned regularizer can bring to the PSM scheme, and the improvement over much more complex and slower state-of-the-art methods. Recent variations on RED such as in [22], and PnP methods (as covered in [20]) have improved over the original methods in reconstruction quality in various static imaging problems and/or in theoretical guarantees. However, theoretical guarantees for the case of a non-convex data fidelity term have been provided recently for only one such non-convex scenario - phase-retrieval [23]. As this is the first work to extend RED to spatio-temporal imaging with a PSM model, and to provide a convergence guarantee for the method in the non-convex bilinear scenario, we chose to limit our attention in this paper to the original RED version [17], [24].

B. Previous Work on Dynamic Imaging

Previous work [25], [26] on time-sequential sampling of bandlimited spatio-temporal signals provided an optimal view angle order for the scan and theoretical guarantees for unique and stable reconstruction. However, the approach is limited by its bandlimitedness assumptions.

Several methods [27], [28] recover the underlying motion field from projections using the Radon transform properties. However, these methods require the object information a priori. Other algorithms [29]–[31] alternate between estimating the motion field and the time-varying object. However these methods assume the total density to be preserved over time, which may be a limiting assumption. For instance, imaging a fixed slice of a 3D time-varying object under compression may violate this assumption due to cross-slice motion.

On the other hand, a model-based iterative reconstruction method [32] for dynamic synchrotron CT incorporates a spatiotemporal Markov random field object prior, and models measurement imperfections, and noise characteristics. An interleaved projection acquisition scheme is also proposed.

Another method [33] proposes a multi-agent consensus equilibrium [34]-based technique using multiple deep denoisers for different spatial directions for dynamic cone beam CT.

In dynamic tomography and MRI, partially separable models (PSM) with a particular low-rank form partially separating the spatial and temporal structure have been used to represent the underlying object [11]–[16] and the time-sequential projections [9], [10]. The projection-domain PSM in [9], [10] carries the PSM to the projection domain using the harmonic representation of projections, and provides uniqueness and stability analysis for the problem. In spite of this advantage of the projection domain PSM over its object-domain counterparts, the performance of this approach is still limited by the null space of the measurement operator.

A different PSM-based method for dynamic MRI [35] has a hybrid objective with a PSM model in the data fidelity term and uses the object in a simple l_1 -norm sparsity penalty, with an additional term to penalize the mismatch between the PSM and the object. The method uses a fixed temporal basis initialization with the assumption of achieving temporal Nyquist sampling rate which is not possible for the time-

sequential scenario considered in this work. It does not use an initial guess for the spatial basis functions.

Other PSM-based methods for dynamic MRI [35] and tomography [36] impose the low-rank structure as a soft-constraint with hybrid objectives. The dMRI method [35] uses PSM in the data fidelity term, and uses the object in a basic l_1 -norm sparsity penalty, with an additional term to penalize the mismatch between the PSM and the object. The method does not use a guided initial guess for the object or for the PSM basis functions. The dynamic tomography technique [36] instead uses the object in both the data fidelity term and in a simple total-variation regularizer, with a penalty for object-PSM mismatch, thus providing additional flexibility in the variational model. The method employs a fast initialization scheme using the projection domain PSM algorithm [9], [10].

A recent dMRI method [37] partitions the dynamic object into temporal subsets each lying on a low-dimensional manifold, approximated by its tangent subspace. As a result, the object is represented by a temporally partitioned PSM. A simple sparsity penalty is used for the spatial representation. The spatial basis functions and linear transformations aligning the temporal subsets are determined by optimizing a non-convex objective using an ADMM algorithm, without a convergence analysis. The subset temporal bases are estimated separately from training data, which, in some applications, may not be available. The temporal partitioning uses a heuristic criterion applied to an initial reconstruction.

In an earlier dynamic tomography method [38], the object is decomposed into a low-rank and a sparse component, and the low rankness is enforced implicitly using the nuclear norm. The method assumes the object as static for a set of projections. Other works perform various similar decompositions for dMRI [39]–[42]. A related fast dMRI method [43] decomposes the object representation into three components: the mean signal, a low-rank PSM, and the residual, which is assumed to be sparse in the Fourier domain. Then, each component is estimated in order. Although benchmark competing methods are either faster or more accurate on some of the diverse data sets used for the comparison in [43], the method provides the lowest reconstruction error and runtimes when these quantities are averaged over these data sets.

Recently, object-domain deep image prior (DIP)-based algorithms [18], [44] have been proposed for dynamic MRI. Providing impressive results, DIP-based algorithms such as [18] suffer from overfitting and usually require handcrafted early stopping criteria during the optimization of generator network parameters. To overcome these drawbacks, [44] includes regularization constraining the geodesic distances between generated objects in proportion to the distances between their latent representation. However, this requires the computation of the Jacobian of the generator network at each iteration of the update of the weights, and significantly increases the computational load and run time.

A different approach [45] combines partially separable and generative models. It employs spatial and temporal regularization by penalizing the generator weights and a particular initialization scheme for the inputs to the generator networks. Although it combines the PSM with the recent DIP frame-

work, this method has the following limitations, which are overcome by the proposed approach: (i) The spatial generator is an artifact removal network taking the full-sized spatial basis functions as input. Since this prevents a patch-based implementation, it may be computationally problematic for high-resolution 3D+temporal settings. (ii) The CNN prior for natural images may not be useful as a prior for the individual spatial basis functions, since the least-squares optimal spatial basis functions are the left singular vectors of the complete object, and as such may not have the structure of natural images. (iii) As with the other DIP-based methods, if the additional penalty on the generator parameters is insufficient, this method can be prone to overfitting.

Recently, a neural field-based technique [46] was proposed for dynamic photoacoustic tomography (PACT). The authors use a neural field to represent the dynamic object with a considerably reduced number of parameters. Then, they combine this representation with a simple total variation (TV)-based regularizer and compare the method with the full-rank representation of the object and TV or low-rank inducing priors. Despite providing an efficient representation for the dynamic object, the method overperforms its comparison benchmarks only in some of the view-per-frame settings.

C. Contributions

- 1) To the best of our knowledge, RED-PSM is the first PSM-based approach to dynamic imaging, that uses a pre-trained, learned (RED-based [17]) spatial prior.
- 2) We are not aware of any prior work that uses RED with an explicit low-rankness constraint. In RED-PSM we are able to achieve a parsimonious representation for the dynamic object using PSM while incorporating the RED prior, reducing the data requirements further.
- 3) Unlike supervised methods for spatio-temporal imaging [47]–[51] that learn a spatio-temporal model from training data, RED-PSM does not require ground-truth spatio-temporal training data, which is often not available or expensive to acquire. Thus RED-PSM offers the best of both worlds: a learned spatial model using readily available *static* training data, and unsupervised single-instance adaptation to the spatio-temporal measurement.
- 4) A novel and effective ADMM algorithm for the resulting new minimization problem enforces PSM as a hard constraint and incorporates the learned RED spatial regularizer.
- 5) The method is supported by theoretical analysis, with a convergence guarantee which is of practical importance. First, it provides a mathematical justification to terminate the algorithm after sufficiently many iterations. Second, it eliminates concerns about the solution degrading after too many iterations as in the case of DIP-based methods. While RED has been applied to problems with nonlinear measurement operators, the convergence of RED has been analyzed in this setting only for the phase retrieval problem [23]. The analysis of RED-PSM is the first convergence result of RED in the bilinear, non-convex scenario. Moreover, no convergence analysis is provided for previous PSM works.

- 6) Compared to a recent DIP-based [18] algorithm, RED-PSM achieves better reconstruction accuracy with orders of magnitude faster run times.
- 7) To improve and speed up the empirical convergence of RED-PSM, we use a particular fast projection-domain PSM initialization scheme [9], [10] for the spatial and temporal basis functions. The accelerated and reliable convergence with this initialization scheme is important for applications (e.g. bio-medical) that require fast turn-around between acquisition and reconstruction.
- 8) A version of the approach with a patch-based regularizer is shown to provide almost equivalent reconstruction accuracy. This makes the proposed method conveniently scalable to high-resolution 3D or 4D settings.

II. PROBLEM STATEMENT

In a 2D setting, illustrated in Figure 1, the goal in the dynamic tomography problem is to reconstruct a time-varying object $f(\mathbf{x}, t)$, $\mathbf{x} \in \mathbb{R}^2$ vanishing outside a disc of diameter D , from its projections

$$g(\cdot, \theta, t) = \mathcal{R}_\theta\{f(\mathbf{x}, t)\}$$

obtained using the Radon transform operator \mathcal{R}_θ at angle θ . Considering time-sequential sampling, in which only one projection is acquired at each time instant, and sampling uniform in time, the acquired measurements are

$$\{g(s, \theta_p, t_p)\}_{p=0}^{P-1}, \quad \forall s, t_p = p\Delta t, \quad (1)$$

where s is the offset of the line of integration from the origin (i.e., detector position), and P is the total number of projections (and temporal samples) acquired. The sampling of the s variable is assumed fine enough and is suppressed in the notation. The angular sampling scheme, the sequence $\{\theta_p\}_{p=0}^{P-1}$, with $\theta_p \in [0, 2\pi]$, is a free design parameter.

Our objective in dynamic tomography is to reconstruct the underlying dynamic object $\{f(\mathbf{x}, t_p)\}_{p=0}^{P-1}$ from the time-sequential projections in (1). The challenge is that because each projection belongs to a different object, the projections in (1) are inconsistent. Therefore, a conventional, e.g., filtered backprojection (FBP) reconstruction as for a static object results in significant reconstruction artifacts. This is to be expected, as the problem is severely ill-posed: an image with

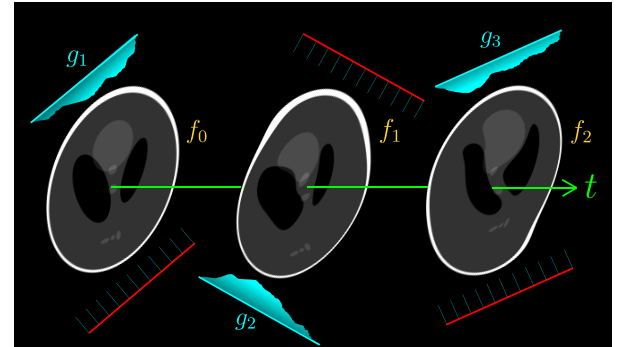


Fig. 1: Imaging geometry for time-varying tomography of the object f_t with single measurement g_t at each instant for $t \in \{0, 1, 2\}$.

a D -pixels diameter requires more than D projections for artifact-free reconstruction, whereas only one projection is available per time-frame in the time-sequential acquisition (1). Multiple dynamic tomography methods [31]–[33] group temporally neighboring projections and assume the object as static during their acquisition. However, this reduces the temporal resolution, and any violation of this assumption (as in the case of time-sequential sampling) leads to mismodeling in the data fidelity terms.

III. PARTIALLY SEPARABLE MODELS (PSM)

For spatio-temporal inverse problems such as dynamic MRI and tomography, the underlying object can be accurately represented using a partially-separable model (PSM), which effectively introduces a low-rank prior to the problem. For dynamic tomography, a PSM can represent the imaged object f , or its full set of projections g . In this paper, we use an object-domain PSM.

The representation of a dynamic object $f(\mathbf{x}, t)$ by a K -th order partially separable model (PSM) is the series expansion

$$f(\mathbf{x}, t) = \sum_{k=0}^{K-1} \Lambda_k(\mathbf{x}) \psi_k(t). \quad (2)$$

This model facilitates interpretability by separating the spatial structure from the temporal dynamics. This expansion is dense in \mathcal{L}_2 [52], meaning that any finite energy object can be approximated arbitrarily well by such a model of sufficiently high order. Empirically, modest values of K provide high accuracy in applications to MR cardiac imaging [12], [53], [54]. Theoretical analysis [10] shows that for a spatially bandlimited object undergoing a time-varying affine transformation (i.e., combination of time-varying translation, scaling, and rotation) of bounded magnitude, a low order PSM provides a good approximation.

As detailed later, we use a d -dimensional representation for the temporal functions, with $d \ll P$. Together with the PSM for the object this leads to a significant reduction in the number of representation parameters for a spatio-temporal object with a D -pixel diameter and P temporal samples: from $\approx PD^2$ to $\approx KD^2 + Kd$, with $K \ll P$. Because $d \ll D$, this corresponds to a factor of $P/K \gg 1$ compression of the representation, providing an effective parsimonious model for the spatio-temporal object f .

Also, by propagating the PSM object model to the projection domain, it enables quantitative analysis [10] of the choice of optimal sequential projection angular schedule.

IV. PROPOSED METHOD: RED-PSM

The overall RED-PSM framework for recovering dynamic objects explained in this section is illustrated in Figure 2.

A. Variational Formulation

We use a discretized version of the PSM (2) for the dynamic object, with the object $f(\cdot, t)$ at each time instant $t = 0, 1, \dots, P-1$, represented by a $N \times N$ -pixel image (a “time frame”, or “snapshot”). Vectorizing these images to

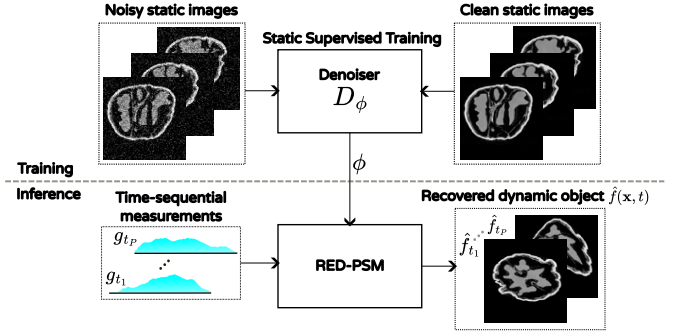


Fig. 2: The RED-PSM framework. The deep denoiser D_ϕ is trained on slices of *static* objects similar to the object of interest, and the learned spatial prior is used at inference time.

vectors $f_t \in \mathbb{R}^{N^2}$, the entire dynamic object is the $N^2 \times P$ matrix $f = [f_0 \dots f_{P-1}]$. It will also be useful to extract individual time frames from f . Denoting the t -th column of the $P \times P$ identity matrix by e_t , we have $f e_t = f_t$, i.e., e_t extracts the t -th column of f . Applying the PSM model, we assume $f = \Lambda \Psi^T \in \mathbb{R}^{N^2 \times P}$, where the columns Λ_k and Ψ_k of $\Lambda \in \mathbb{R}^{N^2 \times K}$ and $\Psi \in \mathbb{R}^{P \times K}$ are the discretized spatial and temporal basis functions for the PSM representation, respectively.

Assuming that the x-ray detector has N bins, the projection of the object at time t is $g_t = g(\cdot, \theta_t, t) = R_{\theta_t} f_t \in \mathbb{R}^N$, where the measurement matrix $R_{\theta_t} \in \mathbb{R}^{N \times N^2}$ computes the projection at view angle θ_t .

We formulate the recovery of f as the solution $\hat{f} = \hat{\Lambda} \hat{\Psi}^T$ to the following variational problem

$$(\hat{\Lambda}, \hat{\Psi}) = \arg \min_{\Lambda, \Psi} \sum_{t=0}^{P-1} (\|R_{\theta_t} \Lambda \Psi^T e_t - g_t\|_2^2 + \lambda \rho(\Lambda \Psi^T e_t)) + \xi \|\Psi\|_F^2 + \xi \|\Lambda\|_F^2 \quad \text{where } \Psi = UZ. \quad (3)$$

The first term is the data fidelity term measuring the fit between available undersampled measurements g_t of the true object and the measurements obtained from the estimated object $f = \Lambda \Psi^T \in \mathbb{R}^{N^2 \times P}$. The second term with weight $\lambda > 0$ is a *spatial* regularizer injecting relevant spatial prior to the problem. It is applied to the PSM $\Lambda \Psi^T$ column by column, that is, to individual temporal image frames. The last two terms with weight $\xi > 0$ prevent the bilinear factors from growing without limit.

Finally, the identity $\Psi = UZ$ is an implicit *temporal* regularizer that restricts the temporal basis functions Ψ to a d -dimensional subspace of \mathbb{R}^P spanned by a fixed basis $U \in \mathbb{R}^{P \times d}$ where $d \geq K$. The action of U on columns of Z may be interpreted as interpolation from d samples to the P -sample temporal basis functions. In practice, we incorporate this identity by explicit substitution (reparametrization of Ψ in terms of the free variable $Z \in \mathbb{Z}^{d \times K}$) into the objective, and the minimization in (3) over Ψ is thus replaced by minimization over Z . This reduces the number of degrees of freedom in Ψ to a fixed number dK , independent of the number P of temporal sampling instants. For notational conciseness, we do not display this constraint/reparametrization in the sequel, but it is used throughout.

B. Incorporating Regularization by Denoising

For the spatial regularizer $\rho(\cdot)$ we consider ‘‘Regularization by Denoising (RED)’’ [17]. RED proposes a recovery method using a denoising operator $D : \mathbb{R}^{N^2} \rightarrow \mathbb{R}^{N^2}$ in an explicit regularizer of the form

$$\rho(f_t) = \frac{1}{2} f_t^T (f_t - D(f_t)). \quad (4)$$

Recent studies using this regularizer provide impressive performances for various *static* image reconstruction tasks including high-dimensional cases [55] and phase retrieval [56]. This regularizer was also combined with a DIP-based fidelity term in [57]. However, we avoid this due to disadvantages related to speed, overfitting, and convergence guarantees.

While it provides significant flexibility for the type of denoisers that can be used, RED still requires D to be differentiable and locally homogeneous, and to satisfy the passivity condition $\|D(f_t)\| \leq \|f_t\|$, for the theoretical analysis of RED to apply.¹

Next, we consider the optimization in (3). For the conventional variational formulation

$$\hat{f}_t = \arg \min_{f_t} \|R_{\theta_t} f_t - g_t\|_2^2 + \lambda \rho(f_t),$$

an efficient choice are iterative algorithms [17] that use the standard ‘‘early termination’’ approach [58], and only require a single use of the denoiser per iteration. However, the regularized PSM objective in (3) does not allow to propagate the RED updates on f to the respective basis functions efficiently. To overcome this difficulty, we perform a bilinear variable splitting $f = \Lambda \Psi^T$ and obtain our final formulation

$$\min_{f, \Lambda, \Psi} H(f, \Lambda, \Psi) \quad \text{s.t.} \quad f = \Lambda \Psi^T \quad (5)$$

$$\text{where } H(f, \Lambda, \Psi) = \sum_{t=0}^{P-1} \left(\left\| R_{\theta_t} \Lambda \Psi^T e_t - g_t \right\|_2^2 + \lambda \rho(f e_t) \right) + \xi \|\Lambda\|_F^2 + \xi \|\Psi\|_F^2. \quad (6)$$

Since the PSM is enforced as a hard constraint, the estimated object f is constrained to have $\text{rank}(f) \leq K$. Problem (5) is non-convex even if ρ is convex, because of the product between unknowns Λ and Ψ .

We propose an algorithm based on ADMM to solve (5). To this end, we form the augmented Lagrangian in the scaled form, [59], [60]

$$\begin{aligned} \mathcal{L}_\beta[\Lambda, \Psi, f; \gamma] = & \sum_t \left(\left\| R_{\theta_t} \Lambda \Psi^T e_t - g_t \right\|_2^2 + \lambda \rho(f e_t) \right) \\ & + \xi \|\Psi\|_F^2 + \xi \|\Lambda\|_F^2 - \frac{\beta}{2} \|\gamma\|_F^2 + \frac{\beta}{2} \|\Lambda \Psi^T - f + \gamma\|_F^2, \end{aligned} \quad (7)$$

where $\gamma \in \mathbb{R}^{P \times N^2}$ represents the scaled dual variable associated with the constraint $f = \Lambda \Psi^T$ and $\beta > 0$ is the penalty parameter.

Then, ADMM can be used to solve (7) as in Algorithm 1.

¹While many powerful denoisers have been demonstrated to satisfy these conditions in [17], recent work [24] provides another framework to explain the good performance of RED with denoisers not satisfying them.

Algorithm 1 RED-PSM

input: $\Lambda^{(0)}, \Psi^{(0)}, \gamma^{(0)}, f^{(0)} = \Lambda^{(0)} \Psi^{(0)T}$, $\beta > 0$, $\lambda > 0$, $\xi > 0$

- 1: **for** $i \in \{1, \dots, I\}$ **do**
- 2: $\Lambda^{(i)} = \arg \min_{\Lambda} \left\{ \sum_t \|R_{\theta_t} \Lambda \Psi^{(i-1)T} e_t - g_t\|_2^2 + \frac{\beta}{2} \|\Lambda \Psi^{(i-1)T} - f^{(i-1)} + \gamma^{(i-1)}\|_F^2 + \xi \|\Lambda\|_F^2 \right\}$
- 3: $\Psi^{(i)} = \arg \min_{\Psi} \left\{ \sum_t \|R_{\theta_t} \Lambda^{(i)} \Psi^T e_t - g_t\|_2^2 + \frac{\beta}{2} \|\Lambda^{(i)} \Psi^T + \gamma^{(i-1)} - f^{(i-1)}\|_F^2 + \xi \|\Psi\|_F^2 \right\}$
- 4: $\forall t : f_t^{(i)} = \arg \min_{f_t} \{ \lambda \rho(f_t) + \frac{\beta}{2} \|(\Lambda^{(i)} \Psi^{(i)T} + \gamma^{(i-1)}) e_t - f_t\|_2^2 \}$
- 5: $\gamma^{(i)} = \gamma^{(i-1)} + \Lambda^{(i)} \Psi^{(i)T} - f^{(i)}$
- 6: **end for**

Line 4 in Algorithm 1 then corresponds to the variational denoising for all t of the ‘‘pseudo image frame’’ $(\Lambda^{(i)} \Psi^{(i)T} + \gamma^{(i-1)}) e_t$ with regularization $\lambda \rho(f_t)$. Instead of solving this denoising problem by running an iterative algorithm to convergence, we follow the RED approach [17], [24], and for each t replace the f_t update in Step 4 by a single fixed-point iteration step using the approach of early stopping [58] (Sec. 4.3.2), taking advantage of the gradient rule

$$\nabla \rho(f_t) = f_t - D_\phi(f_t) \quad (8)$$

where D_ϕ is the denoiser. This results in Algorithm 2, which requires only single use of the denoiser per iteration of ADMM. Furthermore, as in Algorithm 1, the modified Line 4 in Algorithm 2 can be performed in parallel for all t .

Algorithm 2 RED-PSM with efficient f step

Notes: Inputs, and Lines 1-3 and 5-6 are the same as Algorithm 1. The f step is applied $\forall t$.

- 4: $\forall t : f_t^{(i)} = \frac{\lambda}{\lambda + \beta} D_\phi(f_t^{(i-1)}) + \frac{\beta}{\lambda + \beta} (\Lambda^{(i)} \Psi^{(i)T} + \gamma^{(i-1)}) e_t$

C. Regularization Denoiser

The regularization denoiser D_ϕ has a deep neural network CNN (DnCNN) [61] architecture and is trained in a supervised manner on a training set of 2D slices $f_i \in \mathbb{R}^{N^2}$, $i = 1, \dots, N$ of one or more *static* objects similar to the object of interest, assuming that such data will be available in the settings of interest. Thus, the RED steps are agnostic to the specific motion type. The training objective for the denoiser is

$$\min_{\phi} \sum_i \|f_i - D_\phi(\tilde{f}_i)\|_F^2 \quad \text{s.t.} \quad \tilde{f}_i = f_i + \eta_i, \quad \forall i, \quad (9)$$

where the injected noise $\eta_i \sim \mathcal{N}(0, \sigma_i^2 I)$ has noise level $\sigma_i \sim \mathcal{U}[0, \sigma_{\max}]$ spanning a range of values, so that the denoiser learns to denoise data with various noise levels.

D. Computational Cost

Space (memory requirements) and time (operation count) complexities for two variants of the RED-PSM bilinear ADMM Algorithm are shown in Table I. The operation counts are for a single outer iteration. As the number of outer iterations typically has a weak dependence on the size of the problem, the scaling shown tends to determine the run time.

Furthermore, thanks to its structure, the algorithm also offers many opportunities for easy parallelization, so that actual runtime can be proportionally reduced by allocating greater computational resources. See the Supplementary Material Section B for the detailed analysis of computational requirements.

The complexities for the proposed Algorithm 2 are given in the first column of Table I. Space complexity is dominated by the storage of Λ , and scales proportionally to image cross-section size in pixels N^2 , and the order K of the PSM. The time complexity is dominated by the computations of the gradient with respect to Λ , and scales proportionally to the size N^2P of the spatio-temporal object, PSM order K , and the number M_i of inner iterations used to solve optimization subproblems (Lines 2 and 3 in Algorithm 2).

Finally, in the second column of Table I, we investigate the patch-based version of the proposed algorithm described in Section VI-D6. Given a patch size $N_B \ll N$ and stride $s \leq N_B$, this alternative increases the operation count by $(\frac{N_B}{s})^2$ since it operates on overlapping patches. For example, for the settings in our experiments, $s = \frac{N_B}{2}$, increasing the operation count by a factor of 4. This is a modest price to pay, because this alternative also reduces the space complexity by a factor of $(\frac{N_B}{s})^2$. For example, for $N_B=8$ and $N=128$ as used in our experiments, this corresponds to a reduction by a factor of 144 in space complexity. Thus, this variant of RED-PSM enables scaling for high-dimensional and high-resolution settings.

Complexity	PSM-fidelity	Patch-based
Space	$O(KN^2)$	$O(KN_B^2)$
Time	$O(KN^2PM_i)$	$O(KN_B^2PM_i(\frac{N_B}{s})^2)$

TABLE I: Time and space complexities for two variants of the RED-PSM algorithm for a single outer iteration of the bilinear ADMM. M_i is the number of inner iterations for each iteratively solved subproblem, and $N_B \ll N$, $s \leq N_B$.

V. CONVERGENCE ANALYSIS

In this section, we follow an approach similar to recent work on ADMM for a bilinear model [62] to analyze convergence. We show that under mild technical conditions, the objective in Algorithm 1 is guaranteed to converge (with increasing number I of iterations) to a value corresponding to a stationary point of the Lagrangian, that is, satisfying the necessary conditions for the first order optimality.

In practice, Algorithm 2 with the efficient f step version, which we implemented and used in the experiments reported in Section VI, has better run times, and rapid empirical convergence. However, its analysis requires additional steps, which are not particularly illuminating. Therefore, following the tradition in related analyses [58], [63], we focus on the analysis of the nominal Algorithm 1.

The Frobenius norm penalties on basis functions result, as shown in Appendix A, in the boundedness of the iterates $(f^{(i)}, \Lambda^{(i)}, \Psi^{(i)})$.

Different to [62], our objective function has factorized terms in bilinear form. Also, our analysis includes a proof (similar to [64]) of the boundedness of the iterates to justify the existence of points of accumulation of the iterate sequence, which appears to have been inadvertently left out in [62].

To simplify the notation, we replace the separate computation of the projections of time t -frames in the data fidelity term by using the operator $\bar{R} : \mathbb{R}^{N^2 \times P} \rightarrow \mathbb{R}^{N \times P}$ that computes the entire set of P projections at view angles θ_t of the image frames at times t , $t = 1, \dots, P$ of dynamic image f , i.e., of each of its columns indexed by t , producing $g = \bar{R}f \in \mathbb{R}^{N \times P}$. When applied to the PSM, \bar{R} performs $R_{\theta_t} \Lambda \Psi^T e_t$ for each t . We also aggregate the contribution of the RED regularizer into $\bar{\rho}(f) \triangleq \sum_{t=0}^{P-1} \rho(f_t) : \mathbb{R}^{N^2 \times P} \rightarrow \mathbb{R}$, and the denoiser into $\bar{D} : \mathbb{R}^{N^2 \times P} \rightarrow \mathbb{R}^{N^2 \times P}$, which performs D for each column of f indexed by t . Then, the Lagrangian function with dual variable γ can be rewritten as

$$\mathcal{L}[\Lambda, \Psi, f; \gamma] = \|\bar{R}\Lambda\Psi^T - g\|_F^2 + \lambda\bar{\rho}(f) + \xi\|\Lambda\|_F^2 + \xi\|\Psi\|_F^2 + \beta\langle\gamma, (\Lambda\Psi^T - f)\rangle, \quad (10)$$

where the inner product is defined as $\langle A, B \rangle = \text{Tr}(A^T B)$.

The corresponding augmented Lagrangian is

$$\mathcal{L}_\beta[\Lambda, \Psi, f; \gamma] = \|\bar{R}\Lambda\Psi^T - g\|_F^2 + \lambda\bar{\rho}(f) + \xi\|\Lambda\|_F^2 + \xi\|\Psi\|_F^2 + \beta\langle\gamma, (\Lambda\Psi^T - f)\rangle + \frac{\beta}{2}\|\Lambda\Psi^T - f\|_F^2. \quad (11)$$

Then, we can state the subproblems with respect to each primal variable in Algorithm 1 as

$$S_\Lambda = \|\bar{R}\Lambda\Psi^{(i-1)T} - g\|_F^2 + \xi\|\Lambda\|_F^2 + \frac{\beta}{2}\|\Lambda\Psi^{(i-1)T} - f^{(i-1)} + \gamma^{(i-1)}\|_F^2 \quad (12)$$

$$S_\Psi = \|\bar{R}\Lambda^{(i)}\Psi^T - g\|_F^2 + \xi\|\Psi\|_F^2 + \frac{\beta}{2}\|\Lambda^{(i)}\Psi^T - f^{(i-1)} + \gamma^{(i-1)}\|_F^2, \text{ and} \quad (13)$$

$$S_f = \lambda\bar{\rho}(f) + \frac{\beta}{2}\|\Lambda^{(i)}\Psi^{(i)T} - f + \gamma^{(i-1)}\|_F^2. \quad (14)$$

Algorithm 1 will be shown in Theorem 1 to converge to a stationary point of Problem (5), which is defined below.

Definition 1 (Stationary solution for Problem (5)). The point $W^* = (\Lambda^*, \Psi^*, f^*, \gamma^*)$ is a stationary solution of the problem (5) if it satisfies the stationarity and primal feasibility conditions for the variables of the Lagrangian in (10):

$$\nabla_f \mathcal{L}(\Lambda^*, \Psi^*, f^*; \gamma^*) = \lambda \nabla \bar{\rho}(f^*) - \beta \gamma^* = 0; \quad (15a)$$

$$\nabla_\Lambda \mathcal{L}(\Lambda^*, \Psi^*, f^*; \gamma^*) = (2\bar{R}^T(\bar{R}\Lambda^*\Psi^{*T} - g) + \beta\gamma^*)\Psi^* + 2\xi\Lambda^* = 0; \quad (15b)$$

$$\nabla_\Psi \mathcal{L}(\Lambda^*, \Psi^*, f^*; \gamma^*) = (2\bar{R}^T(\bar{R}\Lambda^*\Psi^{*T} - g) + \beta\gamma^*)^T \Lambda^* + 2\xi\Psi^* = 0; \quad (15c)$$

$$f^* = (\Lambda\Psi^T)^{(*)}. \quad (15d)$$

By its definition, a stationary solution of (5) satisfies the necessary first-order conditions for optimality.

To state Theorem 1, we need to introduce some additional definitions pertaining to the denoiser D used in RED.

Definition 2 (Strong Passivity [17]). A function D is strongly passive if $\|D(f)\| \leq \|f\|$.

Moreover, we assume the gradient rule of RED (8). This is shown to hold true when the denoiser D is assumed locally homogeneous (LH) [17] and Jacobian symmetric (JS) [24]. In [17], it was shown that several popular denoisers are

practically LH, and [24] showed that for (8) to hold for the explicit regularizer ρ in (4), JS is necessary.

In our analysis, we only require the gradient rule to hold, rather than the explicit form (4) of the regularizer. Even for denoisers without LH and JS, the gradient rule can be used to define the fixed point iteration in the algorithm [24], and, more recent works on using denoisers for regularization [65]–[69] (in particular [67]) shows how to learn a denoiser jointly with the gradient so that the gradient rule is satisfied.

Finally, we will also assume Lipschitz continuity of the denoiser with some Lipschitz constant L_D , i.e., $\|D_\phi(f_1) - D_\phi(f_2)\|_2 \leq L_D \|f_1 - f_2\|_2$ for all images $f_1, f_2 \in \mathbb{R}^{N^2}$. This means that the denoiser has some finite gain L_D , which is satisfied by any reasonable denoiser.

Our main convergence result is the following.

Theorem 1. *Suppose that the denoiser D_ϕ satisfies the gradient rule in (8), is Lipschitz continuous with some Lipschitz constant L_D , and strongly passive.*

Then, if $\beta > 2L$ where $L \triangleq \lambda(1 + L_D)$, Algorithm 1 converges globally (i.e., regardless of initialization) to a stationary solution (f^, Λ^*, Ψ^*) of (5) in the following sense:*

- (i) The sequence of values of the objective H converges to a limit $H^* = H(f^*, \Lambda^*, \Psi^*)$; and*
- (ii) The iterates generated by Algorithm 1 converge subsequentially to a stationary solution $(f^*, \Lambda^*, \Psi^*, \gamma^*)$ of (5), that is, any accumulation point (of which there is at least one) of the sequence $(f^{(i)}, \Lambda^{(i)}, \Psi^{(i)}, \gamma^{(i)})$ is a stationary solution of (5).*

The proof of Theorem 1 is provided in Appendix A.

Regarding convergence to the globally optimal solution, more can be said. Problem (3) is non-convex even if $\bar{\rho}$ is convex, because of the product between unknowns Λ and Ψ . However, similar to [63], thanks to the inclusion of the Frobenius norms of the factors Λ and Ψ in the bilinear form, when $\bar{\rho}$ is convex (i.e., when LH and JS assumptions hold), the global minimum $\hat{f} = \hat{\Lambda} \hat{\Psi}^T$ of (3) can be shown to coincide with the global minimum in

$$\begin{aligned} \hat{f} = \arg \min_f \sum_{t=0}^{P-1} \|R_{\theta_t} f_t - g_t\|_2^2 + \lambda \bar{\rho}(f) + 2\xi \|f\|_* \\ \text{s.t. rank}(f) \leq K, \end{aligned} \quad (16)$$

where the penalty weight $\xi > 0$ is identical to the Frobenius norm penalty in our RED-PSM objective (5).

Problem (16) is non-convex too, because of the rank constraint. However, consider the convex version of this problem, without the rank constraint, and denote its solution by \hat{f}^{Convex} . If $\text{rank}(\hat{f}^{\text{Convex}}) \leq K$ then the low-rank constraint in Problem (16) is not active, and $\hat{f}^{\text{Convex}} = \hat{f}$. It then follows [63] that the optimality conditions of the convex problem can be used to assess the global optimality of the solution $\hat{f} = \hat{\Lambda} \hat{\Psi}^T$

produced by the algorithm.²

VI. EXPERIMENTS

A. Datasets

Three categories of data sets are used in this work.

Walnut Dataset: We use the CT reconstructions of two different (static) walnut objects from the publicly available 3D walnut CT dataset [71]. We create a dynamic test object by synthetically warping the central axial slice of one of the walnut objects using a sinusoidal piecewise-affine time-varying warp [72]. To be precise, the image is divided into a $N \times N$ uniformly spaced rectangular grid, and the following vertical displacement is applied on each row separately to drive the temporally varying warp $\Delta_{n,t} = -C(t) \sin(3\pi n/N)$, $n \in \{0, \dots, N-1\}$, where $C(t)$ is a linearly increasing function of t and $C(0) = 0$. Static axial, coronal, and sagittal slices of the other walnut object are used to train the denoiser D_ϕ .

Compressed Object Dataset: The compressed object data set is obtained from a materials science experiment [73] with a sequence of nine increasing compression (loading) steps applied to an object, with a full set of radiographic projections collected (using Carl Zeiss Xradia 520 Versa) and reconstructed by the instrument's software at each step. Using this quasi-static data set, a fixed axial slice is extracted from each of the 9 reconstructions. These nine extracted slices corresponding to nine time points are interpolated to P time frames using a recent deep learning-based video interpolation algorithm [74]. The denoiser D_ϕ for our experiments on this data set was trained using the axial slices of the static pre-compression and post-compression versions of the object, which would be available in actual dynamic loading experiments of this type.

In a conference submission [75] citing this work, the method has been applied (without describing the algorithm or its theory) to additional tomographic scenarios of materials compressed under load, further confirming the advantage of the proposed method and algorithm over the compared methods.

We note that all algorithms compared in this paper are agnostic to both the synthetic warp applied on the static walnut slice and to the data-driven interpolation method used for the compressed object.

Spatio-temporal projection data for each dataset is simulated by a parallel-beam projection with $N=128$ detector bins of the dynamic phantoms, a single projection at each of the P time instants. The sequence of projection angles $\{\theta_t\}_{t=0}^{P-1}$ (a free experimental design parameter) was chosen to follow the bit-reversed view angle sampling scheme, which has been shown [9] to provide an especially favorable conditioning of the recovery problem. The simulated measurements are corrupted

²The work in [63] credits an equivalence between minimizing the sum of the Frobenius norm of the factors and the minimization of the nuclear norm of the product to [70]. However, the analysis in [70] is not directly applicable to our scenario. It would require the data fidelity $R_{\theta_t} \Lambda \Psi^T e_t = g_t$ as a hard constraint, includes only the Frobenius norm penalties in the minimization objective without additional explicit regularization, and requires the measurement operator to satisfy a Restricted Isometry Property (RIP). We are not aware of an analysis showing RIP for the measurement models in this paper. These aspects prevent inferring an equivalence between our problem and nuclear norm minimization directly from [70].

using AWGN with standard deviation $\sigma = 5 \cdot 10^{-3}$. This noise level leads to the FBP (with Ram-Lak filter) of the full set of $P=512$ projections at each time instant having a PSNR of approximately 46 dB. When, in the actual experiments with sequentially sampled data, only $1/P$ of this data is used, the PSNR of the reconstruction may be expected to be lower.

Ground-truth frames for $P = 4$ are shown in Figure 3.

Cardiac dMRI Dataset: For a more direct comparison with the setting and data used in dMRI works, we also test RED-PSM on the “retrospective” cardiac dMRI data in [18]. The data includes 23 distinct time frames for one cardiac cycle. Details of the data and experiments are in Section VI-D4.

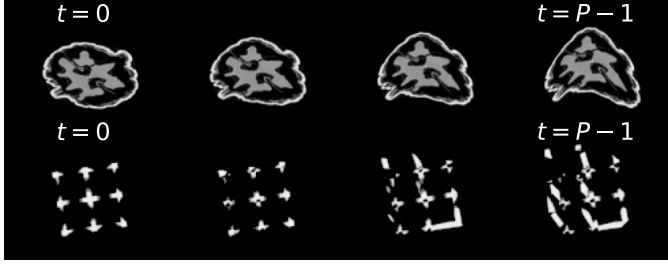


Fig. 3: Ground-truth frames uniformly sampled in time for $P = 4$, for the time-varying walnut (top) and compressed object (bottom).

B. Baseline Methods

PSM-TV: Similar to the proposed approach, this algorithm also uses a PSM to represent the object, but instead of the RED regularizer, the regularization penalizes the discrete 2D total variation of the temporal frames of f at each time instant. To this end, the constraint $f = \Lambda\Psi^T$ is implemented by substitution into the objective in (5), and the definition of ρ is changed to $\rho(\cdot) = \text{TV}(\cdot)$, and the rest of the objective is kept the same. We consider spatial (PSM-TV-S) and spatiotemporal (PSM-TV-ST) alternatives of TV. The former computes TV only spatially in a single frame at each t whereas the latter also computes differences between temporally adjacent pixels at $t - 1$ and $t + 1$. The unconstrained problem is then solved for $\{\hat{\Lambda}, \hat{\Psi}\}$ (using Adam optimizer in Pytorch). Finally, the estimated object is obtained as $\hat{f} = \hat{\Lambda}\hat{\Psi}^T$.

TD-DIP [18]: TD-DIP is a recent method based on the Deep Image Prior (DIP) approach.³ It uses a mapping network M_α and a generative model N_β in cascade to obtain the estimated object at each time instant f_t from fixed and handcrafted latent representations χ_t . Because TD-DIP was originally proposed for dynamic MRI, we modified the objective minimally for dynamic tomography as

$$\min_{\alpha, \beta} \sum_t \|g_t - R_{\theta(t)}((N_\beta \circ M_\alpha)(\chi_t))\|^2. \quad (17)$$

For the comparisons in this work, identical mapping network and generator architectures, latent representation dimensionality, optimizer, learning rate, and decay schemes are used as in the available implementation [76]. The original work focuses on the beating heart problem and thus proposes a helix-shaped

³It would be interesting to include yet another baseline (also developed for dMRI) – the DIP-based PSM approach [45]. However, as an implementation of this method was unavailable, and due to potential issues (specific initialization and framework that use other MRI algorithms) with replicating its performance and adapting to our CT problem, we were unable to do so.

manifold for χ_t with number of cycles equal to the number of heartbeats during measurement acquisition. Since we do not have a repetition assumption for the motions of the walnut and compressed object, we use a linear manifold as explained in the original paper [18]. Thus, for clarity, in Section VI-D the method is sometimes denoted as “TD-DIP (L)”.

C. Experimental Settings

All methods are run on a workstation with an Intel(R) Xeon(R) Gold 5320 CPU and NVIDIA RTX A6000 GPU. In practice, we used a minor variation of Algorithm 2, where we combined the subproblems for Λ and Ψ , and minimized with respect to both basis functions simultaneously using gradient descent with Adam [77] optimizer.

Denoiser and training. Each convolutional layer in the denoiser network is followed by a ReLU nonlinearity except for the final single-channel output layer. We tested both direct and residual DnCNN denoisers, where the former predicts the denoised image and the latter estimates the noise from the input. We use the denoiser type that performs better for each object, but the differences are minor. Further architectural details for the denoisers in our experiments are provided in Table VII in the Supplementary Material. We use three pre-trained denoisers, one for each of the three object types. In each case, the same pre-trained denoiser was used for all values of P .

The upper limit for noise level used in training the denoiser was set to $\sigma_{\max} = 5 \cdot 10^{-2}$. For the dynamic walnut object, the denoiser D_ϕ is trained on the central 200 axial, 200 sagittal, and 200 coronal slices of another static walnut CT reconstruction downsampled to size 128×128 . For the compressed object, axial slices of pre-compression and post-compression static versions of the object, containing 462 slices in total, are used to train D_ϕ . For the cardiac MRI setting, the denoiser was trained on the static MRI training slices of the ACDC dataset [78]. For all datasets, D_ϕ is trained for 500 epochs using the Adam optimizer with a learning rate of $5 \cdot 10^{-3}$. We test both direct and residual DnCNN denoisers where the former predicts the denoised image and the latter estimates the noise from the input.

Architectural details for denoisers in our experiments are provided in Table VII in Supplementary Material A. We use a fixed pre-trained denoiser for all P for the same object type.

Temporal Basis. In compressed material and cardiac dMRI data experiments, we use the parametrization $\Psi = UZ$ with a fixed basis U that corresponds to a cubic spline interpolator, and for the warped walnut we use DCT-II, to interpolate the low-dimensional temporal representation Z to Ψ .

Initialization. Unless stated otherwise, the spatial and temporal basis functions are initialized using the SVD truncated to the rank of the dynamic object estimate produced by a recent projection-domain PSM-based method “ProSep” [10]. If the ProSep estimate has rank smaller than K , the remaining basis functions are initialized as 0.

Otherwise, all spatial basis functions are initialized as 0 and the temporal latent representations z_k are initialized randomly as $z_k \sim \mathcal{N}(0, I)$.

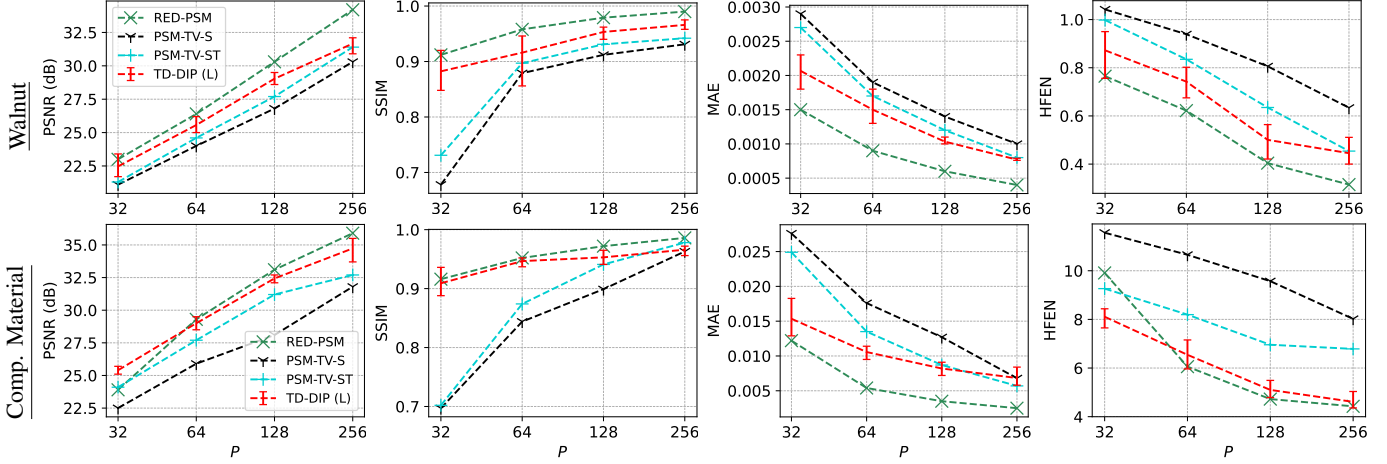


Fig. 4: Reconstruction metrics for the time-varying walnut and compressed material vs. P using different methods. For TD-DIP, the metrics reported are assuming a “stopping oracle” that stops the iterations at the best PSNR reconstruction. The minimum and maximum values over three different runs with different random initial values are shown with bars, and the mean values are connected by dashed lines

Tomographic Acquisition Scheme. All methods mentioned in this paper use the bit-reversed angular sampling scheme, over the range $[0, \pi]$. For time-sequential acquisition, the bit-reversed scheme was shown [9], [10] to provide favorable results via better conditioning of the forward model in comparison to alternatives. In a standard CT scanner, the speed of rotation might have to be significantly increased to implement this scheme, possibly leading to greater motion blur. However, for several scenarios this would not be much of an issue. These include radial acquisition in MRI; a CT scanner with electronic beam deflection [79]; and settings where the acquisition time is dominated by the time to acquire each view rather than the rotation time, e.g., micro-CT, or imaging of dense materials.

To help address the challenge in implementing the bit-reversed scheme in other, more physically constrained settings, the number of distinct view angles \hat{P} can be reduced and these views can be repeated periodically without a performance drop as also shown in Figure 11. With a reduced \hat{P} , the bit-reversed scheme can be implemented more conveniently, e.g., by multiple source-detector pairs, or by carbon nanotube sources [80], [81].

Run Times. For $P = 256$ and using the specified computational resources and parameter settings, to reach the peak PSNR during optimization, RED-PSM with ProSep initialization requires $50 < \text{iterations} < 150$ taking about 2 to 6 minutes whereas TD-DIP with batch size P typically requires $> 30k$ steps, taking about 3.5 hours to complete. Hence, RED-PSM provides a speedup over TD-DIP by a factor of 35 to 105. Depending on the parameter configuration, the speedup factor may vary. However, the proposed method provides a significant run time reduction in all cases.

Evaluation Metrics. Four quantitative metrics were implemented for comparing different method performances : (i) the *peak signal-to-noise ratio* (PSNR) in dB; (ii) the *structural similarity index* (SSIM) [82]; (iii) the *mean absolute error* (MAE); and (iv) the *high-frequency error norm* (HFEN) [83]. The latter is defined as $\text{HFEN}(f, f_\tau) = \|\text{LoG}(f) - \text{LoG}(f_\tau)\|_2$ where LoG is a rotationally symmetric Laplacian of Gaussian filter with a standard deviation of 1.5 pixels.

D. Results

1) *Reconstruction accuracies for different P :* RED-PSM is compared in Figure 4 and Table II with PSM-TV-S, PSM-TV-ST and TD-DIP (using, for both a-periodic objects, a linear latent representation). Parameter configurations for the experiments are provided in Table V in Supplementary Material A. While Figure 4 facilitates the assessment and comparison of trends in the metrics for different P for the various methods, Table II provides the detail for a more precise quantitative comparison. In fact, since the plotted range of metrics such as PSNR in Figure 4 is very large due to varying P , Table II emphasizes important differences between methods for the same P .

Remarks:

1) The scale differences in the MAE and HFEN between the two objects are due to working with un-normalized densities.

2) In all TD-DIP experiments, optimization is stopped early to achieve the best PSNR reconstructions, assuming such a “stopping oracle” is available. In a more realistic setting, in the absence of this oracle, TD-DIP optimization with continued iterations suffers from overfitting, and produces in these experiments degraded results. For instance, for the warped walnut slice with 40k iterations, PSNR, SSIM, and MAE degrade significantly to 19.5 dB, 0.822, and $3.1 \cdot 10^{-3}$ for $P = 32$, and 24.1 dB, 0.824, and $2.1 \cdot 10^{-3}$ for $P = 64$. Thanks to the accurate spatial prior and the convergence properties, we do not encounter such a problem for RED-PSM.

3) Because the performance of TD-DIP varies with initialization, in each experiment we ran it three times, with different random initialization, each time using a “stopping oracle” to obtain the best PSNR for the given initialization. Table II reports the average of the *best PSNR reconstruction accuracies* for TD-DIP in these three runs. Figure 4, complements this information, by showing in addition to the average results, also the best and worst of these runs (still using the stopping oracle to get the best PSNR per run).

As expected, for all methods, the estimates improve with increasing P . In terms of PSNR, the proposed algorithm performs on par with or usually better than TD-DIP (for all but the lowest P on the compressed material object),

and consistently better than PSM-TV-S and PSM-TV-ST. The PSNR improvement of RED-PSM over TD-DIP enhances with increasing P , reaching 2.4 dB for the time-varying walnut with $P = 256$. Moreover, for the other three metrics, SSIM, MAE, and HFEN, the improvement of RED-PSM over other algorithms is more significant. Specifically, the reduction in MAE reaches up to and exceeds %50 for both objects for $P = 256$. These observations are valid for both objects, however RED-PSM provides slightly greater improvement over TD-DIP in the walnut case.

We would like to emphasize the significance of these reconstruction quality improvements by comparing them to some representative examples. TD-DIP reports up to 3 dB PSNR and 0.005 SSIM improvement with respect to an *older* dMRI method in a *single* scenario. While providing comparable PSNR improvements (2.4 dB), we are able to provide four times larger SSIM (0.02) improvements *relative to TD-DIP itself*. Other recent dMRI [44] and dynamic passive acoustic tomography [46] methods improve 1.5 dB, and at most 1 dB and often no improvement over their respective benchmarks, again in single imaging scenario for each method.

Also, based on the run-time improvement ($\sim 3x$) of [44] with respect to TD-DIP, RED-PSM is still much ($\sim 10x$ - $30x$) faster, than [44], and more interpretable.

P	Method	(a) Walnut				(b) Compressed Material			
		PSNR (dB)	SSIM	MAE (1e-3)	HFEN	PSNR (dB)	SSIM	MAE (1e-2)	HFEN
32	PSM-TV-S (R)	21.1	0.678	2.9	1.04	22.5	0.697	2.9	11.6
	PSM-TV-ST (R)	21.3	0.731	2.6	0.99	24.1	0.702	2.5	9.3
	TD-DIP (L)	22.5	0.882	2.1	0.87	25.4	0.909	1.5	8.1
	RED-PSM (Pr)	22.8	0.911	1.5	0.78	23.9	0.916	1.2	9.9
64	PSM-TV-S (R)	24.0	0.879	1.9	0.94	25.6	0.845	1.8	10.7
	PSM-TV-ST (R)	24.6	0.897	1.7	0.83	27.7	0.874	1.3	8.2
	TD-DIP (L)	25.6	0.916	1.5	0.74	29.0	0.947	1.1	6.5
	RED-PSM (Pr)	26.4	0.958	0.9	0.57	29.3	0.952	0.5	6.0
128	PSM-TV-S (R)	26.8	0.912	1.4	0.78	29.2	0.907	1.1	9.6
	PSM-TV-ST (R)	27.7	0.931	1.2	0.63	31.2	0.942	0.9	7.0
	TD-DIP (L)	29.0	0.953	1.0	0.50	32.4	0.953	0.8	5.1
	RED-PSM (Pr)	30.3	0.979	0.6	0.40	33.1	0.972	0.4	4.7
256	PSM-TV-S (R)	30.1	0.934	1.0	0.63	31.9	0.963	0.7	8.0
	PSM-TV-ST (R)	31.4	0.942	0.8	0.45	32.7	0.978	0.6	6.8
	TD-DIP (L)	31.7	0.966	0.8	0.45	34.7	0.966	0.7	4.6
	RED-PSM (Pr)	34.2	0.989	0.4	0.32	35.9	0.986	0.3	4.4

TABLE II: Reconstruction accuracies for different P . Random (R) and ProSep (Pr) initialization for the PSM methods. For TD-DIP, the reported accuracies are for the best PSNR using a “stopping oracle”, averaged over three runs with random initial conditions.

Figure 5 compares the reconstructions for both objects at two different values of t for $P = 256$. As expected, PSM-TV-S performs the worst among the compared methods and provides, for both objects, blurry reconstructions lacking finer details. The TD-DIP reconstructions improve somewhat over PSM-TV-S and PSM-TV-ST, but contain visible noise-like artifacts on the piecewise constant regions of the walnut object, which are alleviated by RED-PSM. This is manifested also in the absolute difference figures, with error for TD-DIP distributed throughout the interior regions of the walnut. Also, around the shell of the walnut, RED-PSM is further able to preserve sharper details. For the compressed material, in comparison to TD-DIP, RED-PSM shows reduced absolute error almost uniformly over the object. This difference is more prominent around the highly dynamic regions of the object,

emphasizing the advantage of the proposed method. For a better understanding of RED-PSM results, we also display the reconstructed spatial and temporal basis Λ and Ψ for a time-varying walnut setting in Supplementary Material C.

Reconstructed x - t “slices” through the dynamic walnut are compared in Figure 6. The location of the x - t slice is highlighted on the $t = 0$ static x - y frame by a yellow line. Consistent with the comparison in Figure 5, RED-PSM provides reduced absolute error values throughout the respective x - t slice. Also, as more apparent on the error figures, TD-DIP leads to higher background errors.

Finally, a zoomed-in comparison of the time-varying walnut object for another time instant for $P = 256$ is provided in Figure 7. The comparison shows the better performance of RED-PSM at recovering the finer details clearly.

2) *PSNR vs. t Comparisons*: To complement the cumulative metrics in Figure 4 and Table II and the “snapshot” qualitative comparisons in Figure 5, we study how the reconstructed image frame PSNRs vary over the reconstructed time interval. The per frame PSNRs (in dB) of the walnut and compressed object reconstructed with $P = 256$ by the different methods are shown in Figure 8 as a function of t . For TD-DIP, the best PSNR obtained using a “stopping oracle” is reported, with the red shading indicating, for each t , the interval between the highest and lowest PSNR in three runs with different random initial conditions. For the warped walnut object, RED-PSM provides consistently better PSNR than the best-case TD-DIP for all t . For the compressed object, the same is true at about 70% of t points. Figure 8 also shows transient effects at the beginning and the end for both objects and all methods. In scenarios such as the object compression experiment, in which the initial and final state are static and could be measured using multiple projections, such transients could be eliminated. Similarly, in quasi-periodic scenarios such as cardiac imaging the effect of such transients would be minimal.

3) *Effect of Initialization*: The initialization of Λ , Ψ , and f plays an important role in the performance and convergence speed of RED-PSM. We observe significant speed-up when rather than a random initialization, we initialize the algorithm with ProSep [9] estimated reconstruction. Figure 9 shows PSNR vs. iterations comparison for different initialization techniques for the dynamic walnut object with $P = 256$. The rest of the parameters were selected identical to those indicated in Supplementary Material Table V. This experiment highlights the advantages of initializing with ProSep estimated basis functions: eliminating the need for multiple runs for a best-case result; and speeding up convergence considerably.

Combined also with the convergent algorithm eliminating the need for a unrealistic stopping oracle and the theoretical analysis, RED-PSM provides improved reliability which is of practical significance.

4) *Cardiac dMRI data experiments*: In this setting, different to previous experiments, we used 4 k -space radial lines (“spokes”) per frame at the bit-reversed angles. We used 1.4 and 2.8 cardiac cycles, with $23 \times 4 = 92$ spokes/cycle, for a total of $P=128$ and $P=256$ spokes. The problem is still severely undersampled compared to the experiment in [18]

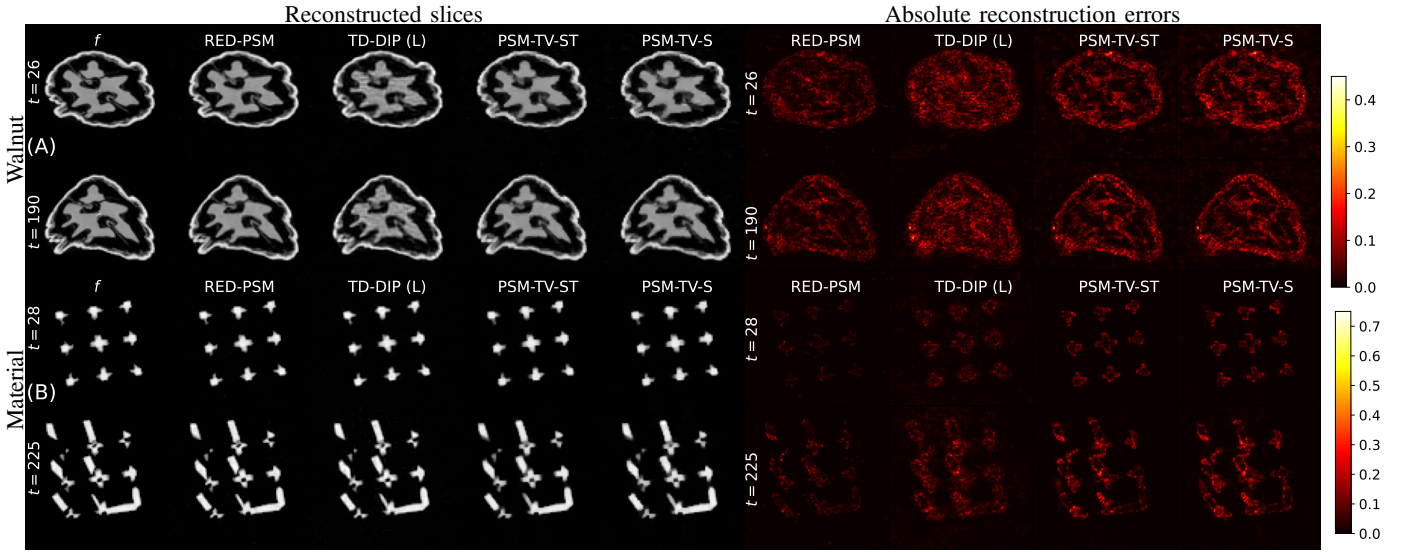


Fig. 5: Comparison of reconstructed object frames at two time instants using different methods for $P=256$, and the corresponding normalized absolute reconstruction errors for (A) the time-varying walnut, and (B) compressed object.

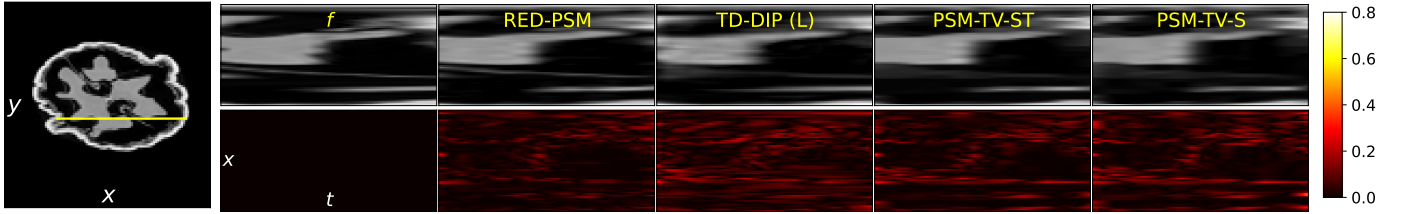


Fig. 6: Comparison of reconstructed $x-t$ slices (top) and corresponding normalized absolute error (bottom) using different methods for $P=256$. The cross-section location is indicated on the static $t = 0$ object with a yellow line. The $x-y-t$ coordinates are indicated in white text on the static object and bottom left absolute error figure.

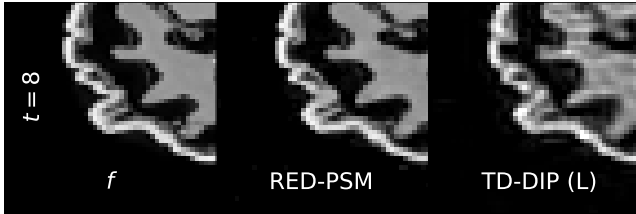


Fig. 7: Zoomed-in walnut reconstruction comparison for $P=256$.

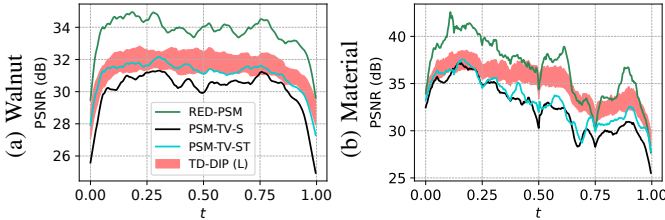


Fig. 8: Reconstruction PSNR vs. t for the (a) time-varying walnut, and (b) compressed material for $P=256$. The red shading for TD-DIP indicates, for each t , the interval between the best and worst PSNR with the early stopping oracle explained in Section VI-D1 in three runs with different random initial conditions.

where 13 spokes are used per frame for 13 cycles, for a total of $13 \times 23 \times 13 = 3,887$ spokes.

Since the data is periodic, we also tested the helix latent scheme (H) for TD-DIP.

The metrics in Table III and the qualitative comparison in Figure 10 with zoomed-in reconstructions and absolute error maps, show that RED-PSM performs better than both versions of TD-DIP.

P	Method	PSNR (dB)	SSIM	MAE (1e-2)	HFEN
128	TD-DIP (L)	34.6	0.923	1.7	3.38
	TD-DIP (H)	34.6	0.928	1.7	3.32
	RED-PSM	36.6	0.939	1.4	2.73
256	TD-DIP (L)	36.2	0.948	1.4	3.47
	TD-DIP (H)	36.4	0.947	1.4	3.44
	RED-PSM	38.4	0.962	1.1	2.99

TABLE III: Reconstruction accuracies for RED-PSM and TD-DIP for the retrospective dMRI data [18].

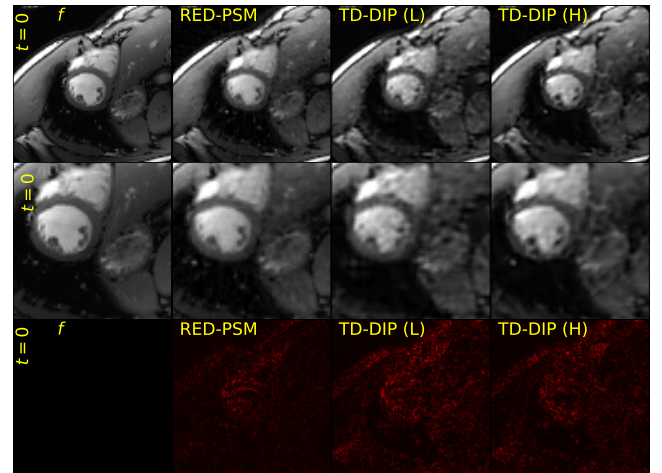


Fig. 10: Reconstructed frames for $P=256$ for retrospective dMRI data [18] with zoomed-in frames (middle row), and absolute reconstruction errors (last row).

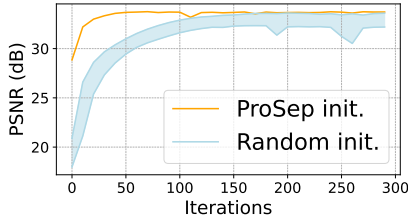


Fig. 9: PSNR vs. iteration comparison for RED-PSM as described in Section VI-C. The area between the best and the worst PSNR for each iteration is shown in blue to highlight the varying performances of five different runs with random initialization.

In [44], the authors compare their method to an *older* version of TD-DIP without the improved latent representation prior scheme for cardiac dMRI and report 1.5 dB PSNR improvement. In RED-PSM, we exceed this improvement on the latest version of TD-DIP in multiple scenarios.

5) *Acquisition with smaller number of distinct view angles*: Since obtaining time-sequential projections from different angles in a sufficiently short time period can be physically challenging, we also test the performance of RED-PSM with an acquisition scheme that may be easier to realize physically: keeping the same total number of P projections, but taken at a smaller number \hat{P} (called “period”) of *distinct* view angles, which are also obtained using the bit-reversed angular sampling scheme. The comparison in Figure 11 shows that it is possible to use up to 1/8-th of the distinct view angles without performance loss for RED-PSM.

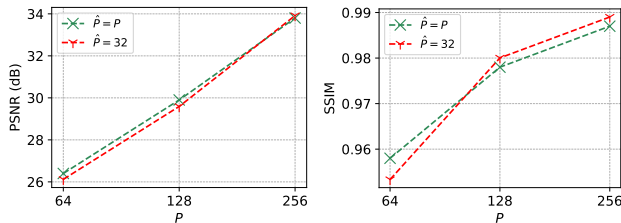


Fig. 11: Reconstruction PSNR and SSIM for the time-varying walnut vs. the number of distinct view angles \hat{P} using RED-PSM with different total number of views P .

6) *Patch-based RED denoiser*: To improve the scalability of the method to higher resolution and/or 3D dynamic object, conveniently, the objective in (5) can be manipulated to operate on the patches of temporal image frames of the time-varying object. This circumvents the need to store the complete image frame at a given time, and also enables the denoiser D_ϕ to be both trained and to operate on patches of image frames, having the potential to incorporate well-known as well as recent techniques [84]–[88].

To showcase the potential of the suggested scheme, we replace the full-size D_ϕ with a patch-based counterpart in the RED step and compare the performance with the originally proposed method for 2D dynamic objects.

The patch-based denoiser for RED updates is trained using

$$\min_{\phi} \sum_i \sum_l \|B_l f_i - D_\phi(B_l \tilde{f}_i)\|_F^2 \text{ s.t. } \tilde{f}_i = f_i + \eta_i, \forall i,$$

where η_i, σ_i are set as in (9), and B_l , with $l \in \{0, \dots, L-1\}$, is the operator to extract the l -th patch of the image. The denoiser D_ϕ operates separately on each patch.

To train the patch-based D_ϕ , uniformly random rotations (multiples of $\frac{\pi}{2}$), and random horizontal/vertical flips, each with $\frac{1}{2}$ probability, were used for data augmentation. The patch size was chosen 8×8 with a stride of 2.

Table IV compares the results for the two denoiser types for both objects, using the same denoiser training policy as in Section VI-C, and experimental configurations of Table VI in the Supplementary Material Section A. The results show little difference, thus verifying the effectiveness of the patch-based version. The analysis of the computational requirements of the patch-based RED-PSM variant in Section IV-D shows its potential for a highly scalable implementation.

We also note that in a divergent beam scenario, the contribution of a patch to a projection will be position dependent and this would require accurate bookkeeping. To this end, there are methods on tile-based approaches in fan-beam [89] and cone-beam [90] tomography. However, we leave such analysis for future studies.

Object	P	Denoiser	PSNR(dB)	SSIM	MAE(1e-3)	HFEN
Walnut	256	Full-image	33.8	0.987	0.4	0.32
		Patch-based	33.7	0.989	0.4	0.35
Material	256	Full-image	35.9	0.986	2.5	4.43
		Patch-based	35.6	0.981	2.7	4.56

TABLE IV: Performance comparison for different denoiser types for RED-PSM. Patch-based denoisers also use DnCNN and have the same configuration and training policy as the full image denoiser.

VII. CONCLUSIONS

We proposed RED-PSM, the first PSM-based approach to dynamic imaging using a pre-trained and learned (RED-based) spatial prior. The objective in the proposed variational formulation is optimized using a novel and effective bilinear ADMM algorithm, which enforces the PSM as a hard constraint. Unlike existing PSM-based techniques, RED-PSM is supported by theoretical analysis, with a convergence guarantee to a stationary point of the objective. The results of the numerical experiments show better reconstruction accuracy and considerably faster run times compared to a recent DIP-based algorithm. A patch-based regularizer version of RED-PSM provides almost equivalent performance with massive reduction of storage requirements, indicating the potential of our framework for dynamic high-resolution 2D or 3D settings.

Possible directions for future work include the application of RED-PSM to different imaging scenarios other than tomography and MRI, and robust denoiser training for RED framework since the deep denoisers encounter varying artifact distributions during optimization. This could also improve the generalizability of the framework to different input types.

Acknowledgements. We thank Dr. Brian M. Patterson for providing the compressed material experiment data.

APPENDIX

In this section, we provide the detailed steps for the proof of Theorem 1.

We begin by establishing some simple consequences of the assumed properties of the denoiser. First, the objective $H(f, \Lambda, \Psi)$ (6) is lower bounded by $\underline{H} \in \mathbb{R}$ because the RED

regularizer $\bar{\rho}(f)$ is non-negative, as follows from the strong passivity assumption on D_ϕ .

$$\begin{aligned}\bar{\rho}(f) &= \langle f, (f - \bar{D}_\phi(f)) \rangle = \|f\|_F^2 - \langle f, \bar{D}_\phi(f) \rangle \\ &= \sum_t \|f_t\|_2^2 - f_t^T D_\phi(f_t) \\ &\geq \sum_t \|f_t\|_2^2 - \|f_t\|_2 \|D_\phi(f_t)\|_2 \geq 0.\end{aligned}\quad (18)$$

$$\geq \sum_t \|f_t\|_2^2 - \|f_t\|_2 \|D_\phi(f_t)\|_2 \geq 0. \quad (19)$$

Second, we have the following result.

Lemma 2. *If the denoiser D_ϕ satisfies the gradient rule in (8) and L_D Lipschitz continuous, then the regularizer $\bar{\rho}(f)$ is gradient Lipschitz continuous with gradient Lipschitz constant $L_{\nabla \bar{\rho}} = 1 + L_D$.*

Proof. Let $f_{(1)}$ and $f_{(2)}$ denote two different spatio-temporal objects. By the gradient rule of ρ , (8), and the assumed L_D Lipschitz continuity of the denoiser D_ϕ we have

$$\begin{aligned}\|\nabla \bar{\rho}(f_{(1)}) - \nabla \bar{\rho}(f_{(2)})\|_F &= \|f_{(1)} - f_{(2)} - (\bar{D}_\phi(f_{(1)}) - \bar{D}_\phi(f_{(2)}))\|_F \\ &\leq \|f_{(1)} - f_{(2)}\|_F + \|\bar{D}_\phi(f_{(1)}) - \bar{D}_\phi(f_{(2)})\|_F \\ &\leq (1 + L_D)\|f_{(1)} - f_{(2)}\|_F.\end{aligned}$$

□

Third, we establish strong convexity of the objectives in the different subproblems in Algorithm 2. Clearly, for any choice of positive constant ξ the objectives S_Λ (12) and S_Ψ (13) in the subproblems for Λ and Ψ are strongly convex with moduli $\alpha_\Lambda \geq \xi$ and $\alpha_\Psi \geq \xi$, respectively.

As we show next, with the assumed $\beta > L$, the objective S_f in (14) is strongly convex too with modulus $\alpha_f \geq \beta - L > 0$.

To prove this, we rewrite $S_f = \omega(f) + \frac{1}{2}(\beta - L)\|f\|_F^2$ where

$$\begin{aligned}\omega(f) &\triangleq \lambda \bar{\rho}(f) + \frac{L}{2}\|f\|_F^2 - \beta \langle f, \Lambda^{(i)} \Psi^{(i)T} + \gamma^{(i-1)} \rangle \\ &\quad + \frac{\beta}{2}\|\Lambda^{(i)} \Psi^{(i)T} + \gamma^{(i-1)}\|_F^2\end{aligned}$$

and show that $\omega(f)$ is a convex function. Since $\frac{1}{2}(\beta - L)\|f\|_F^2$ is convex quadratic for $\beta > L$, it then follows (by one of the alternative definitions of strong convexity) that S_f is a strongly convex function with modulus $\alpha_f \geq \beta - L$.

All that remains, is to show that $\omega(f)$ is a convex function. This follows immediately by recalling Lemma 2, that $\lambda \bar{\rho}(f)$ is gradient Lipschitz continuous with gradient Lipschitz constant $L = \lambda(1 + L_D)$, and applying Lemma 3 below to the first two terms of $\omega(f)$.

Lemma 3. (Thm. 2.1 of [91]) *If $\bar{\rho}(f) : \mathbb{R}^n \rightarrow \mathbb{R}$ is Lipschitz continuously differentiable on a convex set C with some Lipschitz constant L , then $\phi(f) = \bar{\rho}(f) + \frac{1}{2}\beta\|f\|_F^2$ is a convex function on C for every $\beta \geq L$.*

With these preliminaries established, our proof of Theorem 1 follows steps similar to [62](Sec. 4.2), but for our own Algorithm 1:

1. Bounding the size of successive differences of the dual variables by those of the primal ones.

2. Showing that $\mathcal{L}_\beta[f^i, \Lambda^i, \Psi^i; \gamma^i]$, the augmented Lagrangian, is a lower-bounded decreasing function.

3. Combining the first two steps and showing convergence to a stationary solution.

The following result upper bounds the successive differences of the dual variable by those of the primal.

Lemma 4. *Using the update rules in Algorithm 1, the following holds:*

$$\|\gamma^{(i)} - \gamma^{(i-1)}\|_F \leq \frac{L}{\beta} \|f^{(i)} - f^{(i-1)}\|_F, \quad \forall i \geq 1,$$

where $L = \lambda(1 + L_D)$.

Proof. Since $f^{(i)}$ is the optimal solution for Line 4 of Algorithm 1, it should satisfy the optimality condition

$$\begin{aligned}\lambda \nabla \bar{\rho}(f^{(i)}) - \beta(\gamma^{(i-1)} - \Lambda \Psi^{(i)T} + f^{(i)}) &= 0 \\ \lambda \nabla \bar{\rho}(f^{(i)}) - \beta \gamma^{(i)} &= 0\end{aligned}\quad (20)$$

where (20) is due to the dual variable update Step 5 in Algorithm 1. Then, using Lemma 2, we have

$$\begin{aligned}\|\gamma^{(i)} - \gamma^{(i-1)}\|_F &= \frac{\lambda}{\beta} \|\nabla \bar{\rho}(f^{(i)}) - \nabla \bar{\rho}(f^{(i-1)})\|_F \\ &\leq \frac{\lambda}{\beta} (1 + L_D) \|f^{(i)} - f^{(i-1)}\|_F = \frac{L}{\beta} \|f^{(i)} - f^{(i-1)}\|_F.\end{aligned}$$

□

Next, using Lemma 4, we show that the augmented Lagrangian is decreasing and bounded below.

Lemma 5. *In Algorithm 1, if $\beta > 2L$, then the following two propositions hold true.*

1. *Successive differences of the augmented Lagrangian function (11) are bounded above by*

$$\begin{aligned}\mathcal{L}_\beta[f^{(i)}, \Lambda^{(i)}, \Psi^{(i)}; \gamma^{(i)}] - \mathcal{L}_\beta[f^{(i-1)}, \Lambda^{(i-1)}, \Psi^{(i-1)}; \gamma^{(i-1)}] &\leq -C_f \|f^{(i)} - f^{(i-1)}\|_F^2 - C_\Psi \|\Psi^{(i)} - \Psi^{(i-1)}\|_F^2 \\ &\quad - C_\Lambda \|\Lambda^{(i)} - \Lambda^{(i-1)}\|_F^2,\end{aligned}\quad (21)$$

where $C_f = \frac{\alpha_f}{2} - \frac{L^2}{\beta}$, $C_\Lambda = \frac{\alpha_\Lambda}{2}$, and $C_\Psi = \frac{\alpha_\Psi}{2}$ are positive constants. That is, the augmented Lagrangian is monotone decreasing.

2. *There exists an $\underline{\mathcal{L}}_\beta$ such that*

$$\mathcal{L}_\beta[f^{(i)}, \Lambda^{(i)}, \Psi^{(i)}; \gamma^{(i)}] \geq \underline{\mathcal{L}}_\beta.$$

That is, the augmented Lagrangian is lower bounded.

Proof. Part 1.

For conciseness define $W^{(i)} = (\Psi^{(i)}, \Lambda^{(i)}, f^{(i)}; \gamma^{(i)})$. Then the successive difference of the augmented Lagrangian can be expressed by adding and subtracting the term $\mathcal{L}_\beta[\Psi^{(i)}, \Lambda^{(i)}, f^{(i)}; \gamma^{(i-1)}]$,

$$\begin{aligned}\mathcal{L}_\beta[W^{(i)}] - \mathcal{L}_\beta[W^{(i-1)}] &= \mathcal{L}_\beta[W^{(i)}] - \mathcal{L}_\beta[\Psi^{(i)}, \Lambda^{(i)}, f^{(i)}; \gamma^{(i-1)}] \\ &\quad + \mathcal{L}_\beta[\Psi^{(i)}, \Lambda^{(i)}, f^{(i)}; \gamma^{(i-1)}] - \mathcal{L}_\beta[W^{(i-1)}].\end{aligned}\quad (22)$$

For the first two terms on the RHS, using Lemma 4 we have

$$\begin{aligned}\mathcal{L}_\beta[W^{(i)}] - \mathcal{L}_\beta[\Psi^{(i)}, \Lambda^{(i)}, f^{(i)}; \gamma^{(i-1)}] &= \beta \langle \gamma^{(i)} - \gamma^{(i-1)}, (\Lambda \Psi^T)^{(i)} - f^{(i)} \rangle \\ &= \|\gamma^{(i)} - \gamma^{(i-1)}\|_F^2 \leq L^2 \|f^{(i)} - f^{(i-1)}\|_F^2.\end{aligned}\quad (23)$$

where the first equality in (23) follows from the dual variable update in Step (5) of Algorithm 1. The last two terms on the RHS of (22) are further split into

$$\begin{aligned} & \mathcal{L}_\beta[\Psi^{(i)}, \Lambda^{(i)}, f^{(i)}; \gamma^{(i-1)}] - \mathcal{L}_\beta[W^{(i-1)}] \\ &= \mathcal{L}_\beta[\Psi^{(i)}, \Lambda^{(i)}, f^{(i)}; \gamma^{(i-1)}] - \mathcal{L}_\beta[\Psi^{(i)}, \Lambda^{(i)}, f^{(i-1)}; \gamma^{(i-1)}] \\ & \quad + \mathcal{L}_\beta[\Psi^{(i)}, \Lambda^{(i)}, f^{(i-1)}; \gamma^{(i-1)}] \\ & \quad - \mathcal{L}_\beta[\Psi^{(i-1)}, \Lambda^{(i)}, f^{(i-1)}; \gamma^{(i-1)}] \\ & \quad + \mathcal{L}_\beta[\Psi^{(i-1)}, \Lambda^{(i)}, f^{(i-1)}; \gamma^{(i-1)}] - \mathcal{L}_\beta[W^{(i-1)}]. \end{aligned} \quad (24)$$

The first two terms on the RHS of (24) are upper bounded using the strong convexity of S_f with modulus α_f :

$$\begin{aligned} & \mathcal{L}_\beta[\Psi^{(i)}, \Lambda^{(i)}, f^{(i)}; \gamma^{(i-1)}] - \mathcal{L}_\beta[\Psi^{(i)}, \Lambda^{(i)}, f^{(i-1)}; \gamma^{(i-1)}] \\ & \leq \langle \nabla_f S_f[\Psi^{(i)}, \Lambda^{(i)}, f^{(i)}; \gamma^{(i-1)}], f^{(i)} - f^{(i-1)} \rangle \\ & \quad - \frac{\alpha_f}{2} \|f^{(i-1)} - f^{(i)}\|_F^2 = -\frac{\alpha_f}{2} \|f^{(i-1)} - f^{(i)}\|_F^2, \end{aligned} \quad (25)$$

where the last line of (25) is due to the optimality condition of Line 4 of Algorithm 1 for $f^{(i)}$.

The next two terms on the RHS of (24) are upper bounded using the strong convexity of S_Ψ with modulus α_Ψ as

$$\begin{aligned} & \mathcal{L}_\beta[\Psi^{(i)}, \Lambda^{(i)}, f^{(i-1)}; \gamma^{(i-1)}] - \mathcal{L}_\beta[\Psi^{(i-1)}, \Lambda^{(i)}, f^{(i-1)}; \gamma^{(i-1)}] \\ &= S_\Psi(\Lambda^{(i)}, \Psi^{(i)}, f^{(i-1)}; \gamma^{(i-1)}) \\ & \quad - S_\Psi(\Lambda^{(i)}, \Psi^{(i-1)}, f^{(i-1)}; \gamma^{(i-1)}) \\ & \leq \langle \nabla_\Psi S_\Psi[\Psi^{(i)}, \Lambda^{(i)}, f^{(i-1)}; \gamma^{(i-1)}], \Psi^{(i)} - \Psi^{(i-1)} \rangle \\ & \quad - \frac{\alpha_\Psi}{2} \|\Psi^{(i)} - \Psi^{(i-1)}\|_F^2 = -\frac{\alpha_\Psi}{2} \|\Psi^{(i)} - \Psi^{(i-1)}\|_F^2. \end{aligned}$$

Repeating similar steps for the last two terms on the RHS of (24) using the objective S_Λ leads to the upper bound of $-\frac{\alpha_\Lambda}{2} \|\Lambda^{(i)} - \Lambda^{(i-1)}\|_F^2$.

Finally, we establish the positivity of the constants in (21). We have $c_\Psi = \alpha_\Psi \geq \xi > 0$ and $c_\Lambda = \alpha_\Lambda \geq \xi > 0$. Next, because $\alpha_f \geq \beta - L$, we have $C_f = \frac{\alpha_f}{2} - L^2 \geq \frac{\beta - L}{2} - L^2 > 0$, where the last inequality follows by the assumption $\beta > 2L$.

Combining these results, we achieve the inequality in (21), which concludes Part 1.

Part 2. For Part 2, we need to show that the augmented Lagrangian is lower bounded.

$$\begin{aligned} L_\beta[W^{(i)}] &= H(f^{(i)}, \Lambda^{(i)}, \Psi^{(i)}) \\ & \quad + \beta \langle \gamma^{(i)}, (\Lambda \Psi^T)^{(i)} - f^{(i)} \rangle + \frac{\beta}{2} \|(\Lambda \Psi^T)^{(i)} - f^{(i)}\|_F^2 \end{aligned} \quad (26)$$

$$\begin{aligned} & \geq H(f^{(i)}, \Lambda^{(i)}, \Psi^{(i)}) + \langle \lambda \nabla \bar{\rho}(f^{(i)}), (\Lambda \Psi^T)^{(i)} - f^{(i)} \rangle \\ & \quad + \frac{L}{2} \|(\Lambda \Psi^T)^{(i)} - f^{(i)}\|_F^2 \end{aligned} \quad (27)$$

$$\geq H(f^{(i)}, \Lambda^{(i)}, \Psi^{(i)}) + \lambda \bar{\rho}((\Lambda \Psi^T)^{(i)}) - \lambda \bar{\rho}(f^{(i)}) \quad (28)$$

$$= H(\Lambda^{(i)} \Psi^{(i)T}, \Lambda^{(i)}, \Psi^{(i)}). \quad (29)$$

where (27) follows by using (20) to replace the second term of (26) by that of (27) and assuming $\beta > L$, and (28) is due to the gradient Lipschitz continuity of the regularizer $\bar{\rho}(\cdot)$,

$$\lambda \bar{\rho}(\Lambda \Psi^T) \leq \lambda \bar{\rho}(f) + \langle \lambda \nabla_f \bar{\rho}(f), \Lambda \Psi^T - f \rangle + \frac{L}{2} \|\Lambda \Psi^T - f\|_F^2.$$

Then, since we initially showed that our minimization objective in (6) is lower bounded by \underline{H} , we have

$$H(\Lambda^{(i)} \Psi^{(i)T}, \Lambda^{(i)}, \Psi^{(i)}) \geq \underline{H},$$

which leads, by combining with (29), to $L_\beta[W^{(i)}] \geq \underline{\mathcal{L}}_\beta = \underline{H}$ and completes the proof of Lemma 5. \square

By Lemma 5, the sequence $L_\beta[W^{(i)}]$ of augmented Lagrangian values converges. What remains is to address the convergence of the objective H and the sequence of iterates $(f^{(i)}, \Lambda^{(i)}, \Psi^{(i)}, \gamma^{(i)})$ to a stationary solution of (5), which we do in the third and final step of the proof of Theorem 1. We start by showing that the duality gap shrinks to zero.

Lemma 6. Consider Algorithm 1 for solving problem (5). If $\beta > 2L$, then the duality gap goes to zero, i.e.

$$\lim_{i \rightarrow \infty} \|(\Lambda \Psi^T)^{(i)} - f^{(i)}\|_F \rightarrow 0.$$

Proof. Lemma 5 implies that when $\beta > 2L$, the sequence of augmented Lagrangian values is convergent. Thus, the LHS of (21) converges to zero. This also means that each of the norms on the RHS converges to zero to satisfy the inequality. Hence, the following successive differences converge to zero,

$$f^{(i)} - f^{(i-1)} \rightarrow 0; \Lambda^{(i)} - \Lambda^{(i-1)} \rightarrow 0; \Psi^{(i)} - \Psi^{(i-1)} \rightarrow 0.$$

Furthermore, applying Lemma 4, we have $\gamma^{(i)} - \gamma^{(i-1)} \rightarrow 0$. Finally, using the update equation for the dual variable γ , we obtain

$$(\Lambda \Psi^T)^{(i)} - f^{(i)} \rightarrow 0, \quad (30)$$

which completes the proof of Lemma 6. \square

It follows from Lemma 6 that the gap $L_\beta[W^{(i)}] - H(\Lambda^{(i)} \Psi^{(i)T}, \Lambda^{(i)}, \Psi^{(i)})$ between the augmented Lagrangian and the objective converges to zero, and therefore thanks to the convergence of $L_\beta[W^{(i)}]$, the objective H too converges. This establishes Part (i) of Theorem 1.

Turning to Part (ii) of Theorem 1, we first show that the iterates are bounded.

Lemma 7. The iterates $(f^{(i)}, \Lambda^{(i)}, \Psi^{(i)}, \gamma^{(i)})$ of Algorithm 1 for solving (5) are bounded for $i > 0$.

Proof. We use the following facts:

(F1) $\mathcal{L}_\beta[W^{(i)}]$ is a non-increasing function as i increases for all $i > 0$, as shown in Lemma 5.

(F2) The objective $H(f, \Lambda, \Psi)$ is coercive with respect to the second and the third variables.

It follows from (F1) that $\mathcal{L}_\beta[W^{(i)}] \leq \mathcal{L}_\beta[W^{(0)}]$, $\forall i \geq 0$. Combining this with (29), yields

$$H((\Lambda \Psi^T)^{(i)}, \Lambda^{(i)}, \Psi^{(i)}) \leq \mathcal{L}_\beta[W^{(i)}] \leq \mathcal{L}_\beta[W^{(0)}]. \quad (31)$$

Now, note that by (5), the first variable $(\Lambda \Psi^T)^{(i)}$ in $H((\Lambda \Psi^T)^{(i)}, \Lambda^{(i)}, \Psi^{(i)})$ only appears as the argument of $\bar{\rho}(\cdot)$, and by (19) $\bar{\rho}(\cdot) \geq 0$. This implies by (F2) that $H((\Lambda \Psi^T)^{(i)}, \Lambda^{(i)}, \Psi^{(i)})$ is coercive with respect to $\Lambda^{(i)}$ and $\Psi^{(i)}$. Combining this with the boundedness of H in (31) implies the boundedness of these iterates.

Next, the boundedness of $f^{(i)}$ follows from Lemma 6, since we showed that $\Lambda^{(i)}$ and $\Psi^{(i)}$, thus $(\Lambda\Psi^T)^{(i)}$ are all bounded, and the duality gap shrinks to zero as the iterates progress.

Finally, since all the primary variables are bounded, the augmented Lagrangian is bounded both from below (by Part 2 of Lemma 5) and from above by (31), and the dual variable iterates $\gamma^{(i)}$ appear only in the linear Lagrangian term, they are also bounded.

This concludes the proof of Lemma 7. \square

It follows that the sequences of iterates $\{(f^{(i)}, \Lambda^{(i)}, \Psi^{(i)}, \gamma^{(i)})\}$ has at least one accumulation point $(f^*, \Lambda^*, \Psi^*, \gamma^*)$. Next, we establish the properties of all such accumulation points.

Taking the limit over i in (20) yields (15a).

Next, since $\Lambda^{(i)}$ is optimal for the subproblem in Line 2 of Algorithm 1, we have

$$\begin{aligned} \nabla_{\Lambda} S_{\Lambda}(\Psi^{(i-1)}, \Lambda^{(i)}, f^{(i-1)}; \gamma^{(i-1)}) &= 0 \\ 2\bar{R}^T(\bar{R}\Lambda^{(i)}\Psi^{(i-1)T}\Psi^{(i-1)} - g\Psi^{(i-1)}) \\ + \beta(\Lambda^{(i)}\Psi^{(i-1)T} - f^{(i-1)} + \gamma^{(i-1)})\Psi^{(i-1)} + \xi\Lambda^{(i)} &= 0 \end{aligned}$$

Taking the limit over i yields (15b). Similarly, taking the limit in the optimality condition with respect to $\Psi^{(i)}$, $\nabla_{\Psi} S_{\Psi}(\Psi^{(i)}, \Lambda^{(i-1)}, f^{(i-1)}; \gamma^{(i-1)}) = 0$ yields (15c). Finally, taking the limit with respect to i in (30) verifies (15d). These results complete the proof of Theorem 1. \square

REFERENCES

- [1] E. Maire *et al.*, “20 Hz X-ray tomography during an in situ tensile test,” *International Journal of Fracture*, 2016.
- [2] I. Danad *et al.*, “Static and dynamic assessment of myocardial perfusion by computed tomography,” *European Heart Journal - Cardiovascular Imaging*, vol. 17, no. 8, pp. 836–844, 03 2016.
- [3] P. J. Keall *et al.*, “Acquiring 4D thoracic CT scans using a multislice helical method,” *Phys. Med. Biol.*, vol. 49, no. 10, p. 2053, 2004.
- [4] A. Scanziani *et al.*, “In situ characterization of immiscible three-phase flow at the pore scale for a water-wet carbonate rock,” *Advances in Water Resources*, vol. 121, pp. 446–455, 2018.
- [5] J. O’Connor *et al.*, “Dynamic contrast-enhanced imaging techniques: CT and MRI,” *Brit. J. Radiol.*, vol. 84, pp. S112–S120, 2011.
- [6] B. M. Patterson *et al.*, “In situ x-ray synchrotron tomographic imaging during the compression of hyper-elastic polymeric materials,” *Journal of materials science*, vol. 51, no. 1, pp. 171–187, 2016.
- [7] —, “Synchrotron CT imaging of lattice structures with engineered defects,” *Journal of Materials Science*, vol. 55, no. 25, 2020.
- [8] M. Salerno *et al.*, “Recent advances in cardiovascular magnetic resonance: techniques and applications,” *Circulation: Cardiovascular Imaging*, vol. 10, no. 6, 2017.
- [9] B. Iskender, Y. Bresler, and M. L. Klasky, “Dynamic tomography reconstruction by projection-domain separable modeling,” in *2022 IEEE 14th Image, Video, and Multidimensional Signal Processing Workshop (IVMSP)*. IEEE, 2022.
- [10] B. Iskender, M. L. Klasky, and Y. Bresler, “Dynamic tomography reconstruction by projection-domain separable modeling,” *arXiv:2204.09935*, 2022.
- [11] Z.-P. Liang, “Spatiotemporal imaging with partially separable functions,” in *2007 4th IEEE international symposium on biomedical imaging: from nano to macro*. IEEE, 2007, pp. 988–991.
- [12] J. P. Haldar and Z.-P. Liang, “Spatiotemporal imaging with partially separable functions: A matrix recovery approach,” in *2010 IEEE International Symposium on Biomedical Imaging*, April 2010, pp. 716–719.
- [13] B. Zhao *et al.*, “Low rank matrix recovery for real-time cardiac mri,” in *2010 IEEE international symposium on biomedical imaging: From nano to macro*. IEEE, 2010, pp. 996–999.
- [14] C. Brinegar, S. S. Schmitter, N. N. Mistry, G. A. Johnson, and Z.-P. Liang, “Improving temporal resolution of pulmonary perfusion imaging in rats using the partially separable functions model,” *Magnetic Resonance in Medicine*, vol. 64, no. 4, pp. 1162–1170, 2010.
- [15] J. P. Haldar and Z.-P. Liang, “Low-rank approximations for dynamic imaging,” in *2011 IEEE International Symposium on Biomedical Imaging: From Nano to Macro*. IEEE, 2011, pp. 1052–1055.
- [16] F. Lam, S. D. Babacan, J. P. Haldar, M. W. Weiner, N. Schuff, and Z.-P. Liang, “Denoising diffusion-weighted magnitude mr images using rank and edge constraints,” *Magnetic resonance in medicine*, vol. 71, no. 3, pp. 1272–1284, 2014.
- [17] Y. Romano *et al.*, “The little engine that could: Regularization by denoising (RED),” *SIAM J. Imaging Sci.*, vol. 10, no. 4, pp. 1804–1844, 2017.
- [18] J. Yoo *et al.*, “Time-dependent deep image prior for dynamic MRI,” *IEEE Transactions on Medical Imaging*, vol. 40, no. 12, pp. 3337–3348, 2021.
- [19] S. V. Venkatakrishnan, C. A. Bouman, and B. Wohlberg, “Plug-and-play priors for model based reconstruction,” in *2013 IEEE Global Conference on Signal and Information Processing*, 2013, pp. 945–948.
- [20] U. S. Kamilov, C. A. Bouman, G. T. Buzzard, and B. Wohlberg, “Plug-and-play methods for integrating physical and learned models in computational imaging: Theory, algorithms, and applications,” *IEEE Signal Processing Magazine*, vol. 40, no. 1, pp. 85–97, 2023.
- [21] X. Xu, Y. Sun, J. Liu, B. Wohlberg, and U. S. Kamilov, “Provable convergence of plug-and-play priors with mmse denoisers,” *IEEE Signal Processing Letters*, vol. 27, pp. 1280–1284, 2020.
- [22] R. Cohen, M. Elad, and P. Milanfar, “Regularization by denoising via fixed-point projection (RED-PRO),” *SIAM Journal on Imaging Sciences*, vol. 14, no. 3, pp. 1374–1406, 2021.
- [23] D. Xue *et al.*, “On the convergence of non-convex phase retrieval with denoising priors,” vol. 70, pp. 4424–4439.
- [24] E. T. Reehorst and P. Schniter, “Regularization by denoising: Clarifications and new interpretations,” *IEEE Transactions on Computational Imaging*, vol. 5, no. 1, pp. 52–67, 2018.
- [25] P. Willis and Y. Bresler, “Optimal scan for time-varying tomography. I. Theoretical analysis and fundamental limitations,” *IEEE Transactions on Image Processing*, vol. 4, no. 5, pp. 642–653, 1995.
- [26] N. Willis and Y. Bresler, “Optimal scan for time-varying tomography. II. Efficient design and experimental validation,” *IEEE Transactions on Image Processing*, vol. 4, no. 5, pp. 654–666, 1995.
- [27] D. Robinson and P. Milanfar, “Fast local and global projection-based methods for affine motion estimation,” *Journal of Mathematical Imaging and Vision*, vol. 18, no. 1, pp. 35–54, 2003.
- [28] X. Xiong and K. Qin, “Linearly estimating all parameters of affine motion using radon transform,” *IEEE Transactions on Image Processing*, vol. 23, no. 10, pp. 4311–4321, 2014.
- [29] C. Jailin and S. Roux, “Dynamic tomographic reconstruction of deforming volumes,” *Materials*, vol. 11, no. 8, 2018.
- [30] C. Jailin *et al.*, “Projection-based dynamic tomography,” *Phys. Med. Biol.*, vol. 66, no. 21, p. 215018, 2021.
- [31] G. Zang, R. Idoughi, R. Tao, G. Lubineau, P. Wonka, and W. Heidrich, “Space-time tomography for continuously deforming objects,” 2018.
- [32] K. A. Mohan *et al.*, “TIMBIR: A method for time-space reconstruction from interlaced views,” *IEEE Transactions on Computational Imaging*, vol. 1, no. 2, pp. 96–111, 2015.
- [33] S. Majee *et al.*, “Multi-slice fusion for sparse-view and limited-angle 4D CT reconstruction,” *IEEE Transactions on Computational Imaging*, vol. 7, pp. 448–462, 2021.
- [34] G. T. Buzzard *et al.*, “Plug-and-play unplugged: Optimization-free reconstruction using consensus equilibrium,” *SIAM Journal on Imaging Sciences*, vol. 11, no. 3, pp. 2001–2020, 2018.
- [35] B. Zhao *et al.*, “Image reconstruction from highly undersampled (k, t)-space data with joint partial separability and sparsity constraints,” *IEEE Transactions on Medical Imaging*, vol. 31, no. 9, pp. 1809–1820, 2012.
- [36] B. Iskender, M. L. Klasky, B. M. Patterson, and Y. Bresler, “Factorized projection-domain spatio-temporal regularization for dynamic tomography,” in *ICASSP 2023-2023 IEEE International Conference on Acoustics, Speech and Signal Processing (ICASSP)*. IEEE, 2023, pp. 1–5.
- [37] Y. Djebra *et al.*, “Manifold learning via linear tangent space alignment (LTSA) for accelerated dynamic MRI with sparse sampling,” *IEEE Transactions on Medical Imaging*, 2022.
- [38] H. Gao, J.-F. Cai, Z. Shen, and H. Zhao, “Robust principal component analysis-based four-dimensional computed tomography,” *Physics in Medicine & Biology*, vol. 56, no. 11, p. 3181, 2011.
- [39] S. G. Lingala, Y. Hu, E. DiBella, and M. Jacob, “Accelerated dynamic mri exploiting sparsity and low-rank structure: kt slr,” *IEEE transactions on medical imaging*, vol. 30, no. 5, pp. 1042–1054, 2011.

- [40] B. Trémouhéac, N. Dikaos, D. Atkinson, and S. R. Arridge, "Dynamic mr image reconstruction—separation from undersampled (k, t) -space via low-rank plus sparse prior," *IEEE transactions on medical imaging*, vol. 33, no. 8, pp. 1689–1701, 2014.
- [41] M. Chiew, S. M. Smith, P. J. Koopmans, N. N. Graedel, T. Blumensath, and K. L. Miller, "k-t faster: acceleration of functional mri data acquisition using low rank constraints," *Magnetic resonance in medicine*, vol. 74, no. 2, pp. 353–364, 2015.
- [42] R. Otazo, E. Candes, and D. K. Sodickson, "Low-rank plus sparse matrix decomposition for accelerated dynamic mri with separation of background and dynamic components," *Magnetic resonance in medicine*, vol. 73, no. 3, pp. 1125–1136, 2015.
- [43] S. Babu *et al.*, "Fast low rank column-wise compressive sensing for accelerated dynamic MRI," *IEEE Transactions on Computational Imaging*, 2023.
- [44] Q. Zou *et al.*, "Dynamic imaging using a deep generative storm (GenSToRM) model," *IEEE Transactions on Medical Imaging*, vol. 40, no. 11, pp. 3102–3112, 2021.
- [45] A. H. Ahmed *et al.*, "Dynamic imaging using deep bi-linear unsupervised representation (DEBLUR)," *IEEE Transactions on Medical Imaging*, vol. 41, no. 10, pp. 2693–2703, 2022.
- [46] L. Lozanski, M. A. Anastasio, and U. Villa, "A memory-efficient self-supervised dynamic image reconstruction method using neural fields," *IEEE Transactions on Computational Imaging*, vol. 8, pp. 879–892, 2022.
- [47] A. Hauptmann *et al.*, "Real-time cardiovascular MR with spatio-temporal artifact suppression using deep learning—proof of concept in congenital heart disease," *Magn. Reson. Med.*, vol. 81, no. 2, pp. 1143–1156, 2019.
- [48] J. Schlemper *et al.*, "A deep cascade of convolutional neural networks for MR image reconstruction," in *Information Processing in Medical Imaging: 25th International Conference, IPMI 2017, June 25-30, 2017*. Springer, 2017, pp. 647–658.
- [49] X. Shi *et al.*, "Convolutional LSTM network: A machine learning approach for precipitation nowcasting," *Advances in neural information processing systems*, vol. 28, 2015.
- [50] L. Wang *et al.*, "Spatial-temporal transformer for video snapshot compressive imaging," *IEEE Transactions on Pattern Analysis and Machine Intelligence*, 2022.
- [51] N. Ginio *et al.*, "Efficient machine learning method for spatio-temporal water surface waves reconstruction from polarimetric images," *Measurement Science and Technology*, vol. 34, no. 5, p. 055801, 2023.
- [52] in *Methods of Modern Mathematical Physics*, M. Reed and B. Simon, Eds. Academic Press, 1972.
- [53] S. Ma *et al.*, "Dynamic MRI reconstruction exploiting partial separability and t-SVD," in *2019 IEEE 7th International Conference on Bioinformatics and Computational Biology (ICBCB)*. IEEE, 2019, pp. 179–184.
- [54] —, "Dynamic MRI exploiting partial separability and shift invariant discrete wavelet transform," in *2021 6th International Conference on Image, Vision and Computing (ICIVC)*. IEEE, 2021, pp. 242–246.
- [55] Y. Sun *et al.*, "Block coordinate regularization by denoising," *Advances in Neural Information Processing Systems*, vol. 32, 2019.
- [56] C. Metzler, P. Schniter, A. Veeraraghavan, and R. Baraniuk, "prdeep: Robust phase retrieval with a flexible deep network," in *International Conference on Machine Learning*. PMLR, 2018, pp. 3501–3510.
- [57] G. Mataev, P. Milanfar, and M. Elad, "Deepred: Deep image prior powered by red," in *Proceedings of the IEEE/CVF International Conference on Computer Vision Workshops*, 2019, pp. 0–0.
- [58] S. Boyd *et al.*, "Distributed optimization and statistical learning via the alternating direction method of multipliers," *Foundations and Trends® in Machine Learning*, 2011.
- [59] D. Gabay and B. Mercier, "A dual algorithm for the solution of nonlinear variational problems via finite element approximation," *Computers & mathematics with applications*, vol. 2, no. 1, pp. 17–40, 1976.
- [60] J. Eckstein and D. P. Bertsekas, "On the Douglas—Rachford splitting method and the proximal point algorithm for maximal monotone operators," *Mathematical Programming*, vol. 55, no. 1, pp. 293–318, 1992.
- [61] K. Zhang *et al.*, "Beyond a Gaussian denoiser: residual learning of deep CNN for image denoising," *IEEE Transactions on Image Processing*, vol. 26, no. 7, pp. 3142–3155, 2017.
- [62] D. Hajinezhad and Q. Shi, "Alternating direction method of multipliers for a class of nonconvex bilinear optimization: convergence analysis and applications," *J. Glob. Optim.*, vol. 70, pp. 261–288, 2018.
- [63] M. Udell *et al.*, "Generalized low rank models," *Foundations and Trends® in Machine Learning*, vol. 9, no. 1, pp. 1–118, 2016.
- [64] Y. Wang *et al.*, "Global convergence of ADMM in nonconvex nonsmooth optimization," *Journal of Scientific Computing*, vol. 78, pp. 29–63, 2019.
- [65] R. Cohen *et al.*, "It has potential: Gradient-driven denoisers for convergent solutions to inverse problems," in *Advances in Neural Information Processing Systems*, vol. 34. Curran Associates, Inc., pp. 18 152–18 164.
- [66] S. Hurault, A. Leclaire, and N. Papadakis, "Gradient step denoiser for convergent Plug-and-Play," in *International Conference on Learning Representations, ICLR 2022*.
- [67] R. Fermanian, M. Le Pendu, and C. Guillemot, "PnP-ReG: Learned regularizing gradient for plug-and-play gradient descent," *SIAM Journal on Imaging Sciences*, vol. 16, no. 2, pp. 585–613, 2023.
- [68] A. Berk *et al.*, "Deep proximal gradient method for learned convex regularizers," in *ICASSP 2023 - 2023 IEEE International Conference on Acoustics, Speech and Signal Processing (ICASSP)*, pp. 1–5.
- [69] J. R. Chand and M. Jacob, "Multi-scale energy (MuSE) plug and play framework for inverse problems," *arXiv:2305.04775*, 2023.
- [70] B. Recht, M. Fazel, and P. A. Parrilo, "Guaranteed minimum-rank solutions of linear matrix equations via nuclear norm minimization," *SIAM review*, vol. 52, no. 3, pp. 471–501, 2010.
- [71] H. Sarkissian *et al.*, "A cone-beam X-ray computed tomography data collection designed for machine learning," *Scientific data*, vol. 6, no. 1, p. 215, 2019.
- [72] "Piecewise Affine Transformation," https://scikit-image.org/docs/dev/auto_examples/transform/plot_piecewise_affine.html.
- [73] B. M. Patterson, "Personal communication," 2022.
- [74] F. Reda *et al.*, "FILM: Frame interpolation for large motion," *arXiv preprint arXiv:2202.04901*, 2022.
- [75] B. Iskender, M. L. Klasky, and Y. Bresler, "Dynamic tomography reconstruction via low-rank modeling with a RED spatial prior," *2023 IEEE International Workshop on Computational Advances in Multi-Sensor Adaptive Processing (CAMSAP 2023)*.
- [76] J. Yoo, <https://github.com/jaejun-yoo/TDDIP>, 2021.
- [77] D. P. Kingma and J. Ba, "Adam: A method for stochastic optimization," *arXiv preprint arXiv:1412.6980*, 2014.
- [78] O. Bernard *et al.*, "Deep learning techniques for automatic MRI cardiac multi-structures segmentation and diagnosis: is the problem solved?" *IEEE Transactions on Medical Imaging*, 2018.
- [79] S. Kulkarni, J. A. Rumberger, and S. Jha, "Electron beam CT: A historical review," vol. 216, no. 5, pp. 1222–1228, publisher: American Roentgen Ray Society.
- [80] D. Spronk *et al.*, "Evaluation of carbon nanotube x-ray source array for stationary head computed tomography," vol. 48, no. 3, pp. 1089–1099.
- [81] S. Xu *et al.*, "Volumetric computed tomography with carbon nanotube x-ray source array for improved image quality and accuracy," vol. 2, no. 1, pp. 1–9, number: 1 Publisher: Nature Publishing Group.
- [82] Z. Wang *et al.*, "Image quality assessment: from error visibility to structural similarity," *IEEE Transactions on Image Processing*, vol. 13, no. 4, pp. 600–612, 2004.
- [83] S. Ravishanker and Y. Bresler, "MR image reconstruction from highly undersampled k-space data by dictionary learning," *IEEE Transactions on Medical Imaging*, vol. 30, no. 5, pp. 1028–1041, 2010.
- [84] K. Dabov *et al.*, "Image denoising by sparse 3-D transform-domain collaborative filtering," *IEEE Transactions on image processing*, vol. 16, no. 8, pp. 2080–2095, 2007.
- [85] S. Gu *et al.*, "Weighted nuclear norm minimization with application to image denoising," in *Proceedings of the IEEE conference on computer vision and pattern recognition*, 2014, pp. 2862–2869.
- [86] M. H. Alkinani and M. R. El-Sakka, "Patch-based models and algorithms for image denoising: a comparative review between patch-based images denoising methods for additive noise reduction," *EURASIP Journal on Image and Video Processing*, vol. 2017, no. 1, pp. 1–27, 2017.
- [87] S. Liang, B. Iskender, B. Wen, and S. Ravishanker, "LABMAT: Learned feature-domain block matching for image restoration," in *2021 IEEE International Conference on Image Processing (ICIP)*. IEEE, 2021, pp. 1689–1693.
- [88] G. Vaksman *et al.*, "Patch craft: Video denoising by deep modeling and patch matching," in *Proceedings of the IEEE/CVF International Conference on Computer Vision*, 2021, pp. 2157–2166.
- [89] S. Xiao *et al.*, "O $(n/\sup 2/\log n)$ native fan-beam tomographic reconstruction," in *Proceedings IEEE International Symposium on Biomedical Imaging*. IEEE, 2002, pp. 824–827.
- [90] Y. Bresler and J. Brokish, "Fast hierarchical backprojection for helical cone-beam tomography," in *Proceedings 2003 International Conference on Image Processing*, vol. 2. IEEE, 2003, pp. II–815.
- [91] S. Zlobec, "On the Liu–Floudas convexification of smooth programs," *Journal of Global Optimization*, vol. 32, no. 3, pp. 401–407, 2005.

SUPPLEMENTARY MATERIAL

A. Experimental configurations

The PSM-TV and PSM-RED parameter selections for the experiments listed in Table II are provided in Table V. Likewise, Table VI shows the parameter configurations for the denoiser type comparison experiments for RED in Table IV. Finally, the architectural information for the DnCNN denoisers used throughout this work is in Table VII.

(a) Walnut						(b) Comp. Material					
P	Method	K	d	λ	$\tilde{\lambda}$	β	K	d	λ	$\tilde{\lambda}$	β
32	PSM-TV-S (R)	3	4	5e-2	-	-	3	4	10	-	-
32	PSM-TV-ST (R)	4	5	5e-2	5e-2	-	3	4	1e1	1e2	-
32	PSM-RED (P)	3	7	1e-4	-	1e-4	3	9	5.12e-2	-	1.6e-2
64	PSM-TV-S (R)	3	4	5e-2	-	-	5	6	10	-	-
64	PSM-TV-ST (R)	4	5	5e-2	5e-2	-	5	6	1e1	1e2	-
64	PSM-RED (P)	4	7	1e-4	-	5e-4	5	9	32e-4	-	4e-3
128	PSM-TV-S (R)	5	7	5e-2	-	-	8	9	5	-	-
128	PSM-TV-ST (R)	6	7	5e-2	1e-1	-	8	9	5	5e1	-
128	PSM-RED (P)	6	9	2e-4	-	2e-4	8	11	4e-4	-	2e-3
256	PSM-TV-S (R)	10	11	5e-2	-	-	11	13	10	-	-
256	PSM-TV-ST (R)	10	11	5e-2	5e-2	-	11	13	1e1	1e2	-
256	PSM-RED (P)	10	11	5e-5	-	1e-4	11	13	1e-4	-	1e-3

TABLE V: The parameter selections for the reconstructions in Table II. The latent penalty weight was selected as $\xi=10^{-1}$ for the walnut, and $\xi=10^{-3}$ for the compressed object experiments.

(a) Walnut						(b) Comp. Material			
P	Denoiser	K	d	λ	β	K	d	λ	β
256	Full-image	10	11	5e-5	1e-4	11	13	1e-4	1e-3
256	Patch-based	10	11	5e-5	1e-4	11	13	1e-4	1e-3

TABLE VI: Parameter configurations for the denoiser type study experiments in Table IV.

Dataset	# of layers	# of channels	Denoising
Walnut	6	64	Direct
Compressed material	3	32	Residual
Cardiac dMRI	6	64	Residual

TABLE VII: Denoiser DnCNN configurations for different datasets.

B. Time and space complexity analyses

In this section, we analyze the operation count and storage requirements for the proposed algorithm and its patch-based version.

In this analysis, M_i represents the number of inner iterations for iteratively solved subproblems, assumed common to the different subproblems, and we assume $K \ll N$. Also, $R_{\theta(t)}$ and $R_{\theta(t)}^T$ are implemented as operators, each requiring $O(N^2)$ when applied to a $N \times N$ image or a projection of size N .

1) *Storage requirements for the input quantities*: When calculations are performed sequentially in t as in the following sections, the storage requirements for the primal and dual variables are calculated for f_t , γe_t , $\Psi^T e_t$ and Λ . The storage of the spatial basis functions Λ dominates the overall storage cost at $O(KN^2)$. The space complexity analyses of different subproblems in the following sections consider terms other than these input quantities.

2) *RED-PSM*: Expanding the Λ and Ψ subproblems in Algorithm 2 in t , we have

$$\min_{\Lambda} \sum_t (\|R_{\theta(t)} \Lambda \Psi^T e_t - g_t\|_2^2 + \beta \|(\Lambda \Psi^T - f + \gamma) e_t\|_2^2) + \xi \|\Lambda\|_F^2, \quad (32)$$

and

$$\min_{\Psi} \sum_t \|R_{\theta(t)} \Lambda \Psi^T e_t - g_t\|_2^2 + \xi \|\Psi^T e_t\|_2^2 + \beta \|(\Lambda \Psi^T - f + \gamma) e_t\|_2^2. \quad (33)$$

We first analyze the operation counts for gradients with respect to Λ and $\Psi^T e_t$, respectively.

We note that in these gradient computations, the term $R_{\theta(t)}^T g_t$ is pre-computed and stored before the start of the algorithm, and $(\gamma - f) e_t$ and $(R_{\theta(t)}^T g_t + (\gamma - f) e_t)$ are computed and stored at each bilinear ADMM outer iteration so that they do not contribute to the respective costs in each inner iteration, i.e., their cost does not scale with M_i .

Starting with the gradient of (33) with respect to $\Psi^T e_t$, we have

$$2((R_{\theta(t)} \Lambda)^T (R_{\theta(t)} \Lambda) + \Lambda^T \Lambda + \xi I) \Psi^T e_t - 2(R_{\theta(t)} \Lambda)^T g_t + 2\Lambda^T (\gamma - f) e_t. \quad (34)$$

The overall operation count for this term is $O(KN^2P)$ due to the computation of $R_{\theta(t)} \Lambda^T$ and $\Lambda^T (\gamma - f) e_t$ at each t . These terms do not need to be computed for each inner iteration.

When $\Psi = UZ$ is used, the gradient for Z requires the multiplication of (34) with $U^T e_t$, adding a minor operation count $O(dK)$.

The most efficient implementation in terms of space complexity is the sequential computation of the gradients for each t without increasing the operation count. It is also possible to parallelize the operations along t with the trade-off between the run time and the storage requirements.

Considering sequential computation for each t , the additional storage requirement is $O(NK)$ due to $R_{\theta(t)} \Lambda$.

Next, we consider the gradient of (32) with respect to Λ

$$2\xi \Lambda + \sum_t 2(R_{\theta(t)}^T R_{\theta(t)} + I) \Lambda (\Psi^T e_t) (e_t^T \Psi) + (R_{\theta(t)}^T g_t + (\gamma - f) e_t) (e_t^T \Psi). \quad (35)$$

The operation count for this gradient term is $O(KN^2PM_i)$ due to $R_{\theta(t)}^T R_{\theta(t)} \Lambda (\Psi^T e_t) (e_t^T \Psi)$.

Assuming sequential computations in t , the additional storage requirement is determined by the storage of the terms $R_{\theta(t)}^T R_{\theta(t)} \Lambda$, $R_{\theta(t)}^T R_{\theta(t)} \Lambda (\Psi^T e_t) (e_t^T \Psi)$, and $(R_{\theta(t)}^T g_t + (\gamma - f) e_t) (e_t^T \Psi)$, each requiring $O(KN^2)$.

The operation count for the efficient implementation of the f -step in Line 4 of Algorithm 2 is dominated by the single forward computation of the denoiser for each t , leading to $O(PC_D)$ where C_D is the operation count of the denoiser D_ϕ for a single frame. In addition to the input variables, the only storage requirement is due to the term $\Lambda \Psi^T e_t$ which is $O(N^2)$.

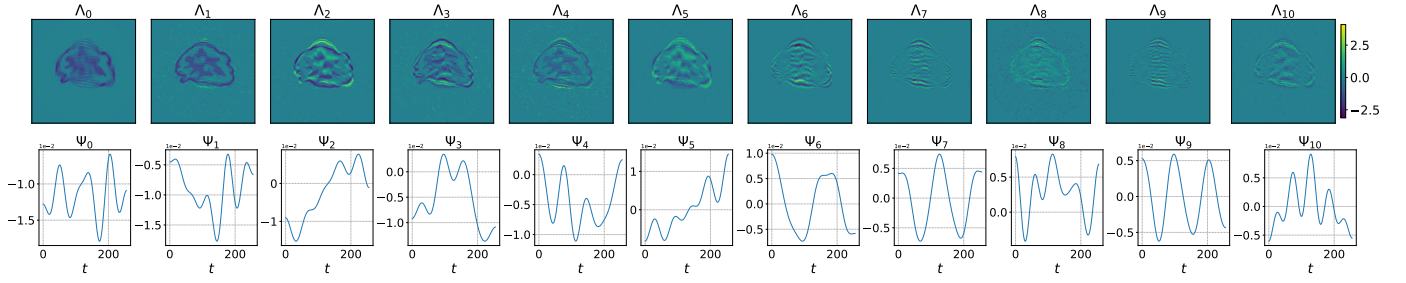


Fig. 12: Reconstructed $K = 11$ spatial (Λ) and temporal (Ψ) basis functions for the time-varying walnut with $P = 256$ and U as DCT-II basis.

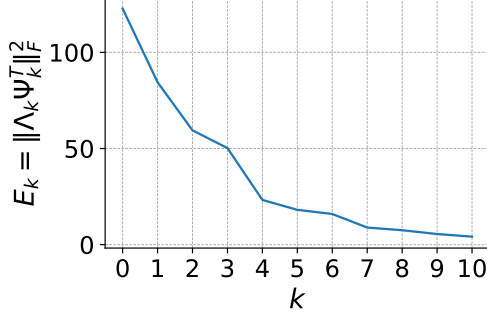


Fig. 13: $E_k = \|\Lambda_k \Psi_k^T\|_F^2$ for each spatiotemporal basis pair for the setting described in Section C.

3) *Patch-based RED-PSM*: The patch-based variant of RED-PSM uses a reduced spatial size N_B for its inputs where $N_B \ll N$. Compared to the originally proposed RED-PSM formulation in (5), the operation count is also dependent on the stride s of the patch extraction operators and the depth of the deep denoiser architecture. Assuming equal-depth or shallower deep convolutional denoisers for patch-based inputs, the total operation count due to the efficient denoiser step stays the same or decreases. Thus, the operation count is again determined by the gradient of the data fidelity term with respect to the patch-based spatial basis functions, and the result approximately scales by the increase in the total stored number of pixels as $O(KN^2PM_i(\frac{N_B}{s})^2)$ where the stride $s \leq N_B$.

The gradients with respect to the data fidelity term require the computation of projections of multiple spatial patches for a given view angle at time t . However, these projections can be computed separately and accumulated. Thus, the space complexity reduces to $O(KN_B^2)$ since we only need to store a single spatial patch of Λ at a given time.

A summary comparison of the two variants of RED-PSM of this section is provided in Section IV-D of the manuscript.

C. Sample reconstructed spatial and temporal basis functions

To help interpret the operation of the proposed RED-PSM algorithm, we display the reconstructed spatial and temporal basis functions Λ and Ψ for the time-varying walnut setting with $P = 256$ and DCT-II latent temporal basis U in Figure 12. The energy corresponding to each basis pair $E_k = \|\Lambda_k \Psi_k^T\|_F^2$ is shown in Figure 13.